

Deep Learning Searches for Vector-Like Leptons at the LHC and Electron/Muon Colliders

António P. Morais,^{1,2,*} António Onofre,^{3,†} Felipe F. Freitas,^{1,2,‡}
João Gonçalves,^{1,2,§} Roman Pasechnik,^{4,¶} and Rui Santos^{5,6,7,**}

¹*Departamento de Física da Universidade de Aveiro, 3810-183 Aveiro, Portugal*

²*Centre for Research and Development in Mathematics and Applications (CIDMA), 3810-183 Aveiro, Portugal*

³*Departamento de Física da Universidade do Minho, 4710-057 Braga, Portugal*

⁴*Department of Astronomy and Theoretical Physics,*

Lund University, Sölvegatan 14A, SE 223-62 Lund, Sweden

⁵*Centro de Física Teórica e Computacional, Faculdade de Ciências,*
Universidade de Lisboa, 1749-016 Lisboa, Portugal

⁶*ISEL - Instituto Superior de Engenharia de Lisboa,*

Instituto Politécnico de Lisboa, 1959-007 Lisboa, Portugal

⁷*Centro de Física Teórica e Computacional, Faculdade de Ciências,*

Universidade de Lisboa, Campo Grande, Edifício C8 1749-016 Lisboa, Portugal

The discovery potential of both singlet and doublet vector-like leptons (VLLs) at the Large Hadron Collider (LHC) as well as at the not-so-far future muon and electron machines is explored. The focus is on a single production channel for LHC direct searches while double production signatures are proposed for the leptonic colliders. Implications for the discovery of VLLs in view of the recently announced muon $(g - 2)_\mu$ anomaly are also discussed. A Deep Learning algorithm to determine the discovery (or exclusion) statistical significance at the LHC is employed. While doublet VLLs can be probed up to masses of 1 TeV, their singlet counterparts have very low cross sections and can hardly be tested beyond a few hundreds of GeV at the LHC. This motivates a physics-case analysis in the context of leptonic colliders where one obtains larger cross sections in VLL double production channels, allowing to probe higher mass regimes otherwise inaccessible even to the LHC high-luminosity upgrade.

* aapmorais@ua.pt

† onofre@fisica.uminho.pt

‡ felipefreitas@ua.pt

§ jpedropino@ua.pt

¶ Roman.Pasechnik@thep.lu.se

** rasantos@fc.ul.pt

I. INTRODUCTION

The Standard Model (SM) of particle physics has, so far, served as the guide towards unraveling the nature of all subatomic phenomena and its success is now indisputable. However, it is clear that it lacks some of the necessary ingredients to fully describe nature, such as an explanation for neutrino masses, as firstly observed in neutrino oscillations by experiments like the Super-Kamiokande [1] or a particle candidate to explain experimental evidences for the existence of Dark Matter (DM) [2]. Recently, other discrepancies have also come into the forefront, such as the measurement of the anomalous magnetic moment of the muon at Fermilab [3], indicating a tension of 4.2σ with the SM predictions, as well as the recent results coming from the LHCb experiment, where hints of lepton flavour universality violation have been reported at a 3.1σ significance [4]. Naturally, such deviations do not meet the 5σ requirement to indicate the existence of new physics (NP) and more data still needs to be collected if the experimental deviations are confirmed. Together with the theoretical calculations in the framework of the SM, an explanation of anomalies requires the addition of NP.

Finding well motivated NP scenarios that simultaneously address all the aforementioned questions is of utmost importance and, in particular, Grand Unified theories (GUTs) provide interesting avenues to follow. These classes of models typically predict new particles present at the TeV scale (or not too far from it), that may be probed at current and future colliders. Therefore, the study of simplified frameworks that can later be mapped to the low-energy limit of a certain UV complete framework can help in constraining their viable parameter space. In particular, some of the authors have proposed a GUT framework, which unifies all matter, Higgs and gauge sectors within the E_8 group, either at a conventional high-scale scenario [5, 6], or a low-scale one [7, 8]. It turns out that, as a common prediction of any of such proposals, the presence of new doublet Vector-Like Lepton (VLL) particles at the TeV scale or below is expected, with relevance for searches at the LHC or near future leptonic colliders. Furthermore, if the anomaly in the measurement of the magnetic moment of the muon is confirmed, which can happen in about one year from the date this article is being written, a possible explanation can arise in the form of TeV scale VLLs.

With the above arguments in mind we study the phenomenological viability of simple extensions of the SM enlarged with a single VLL and a right-handed neutrino. For completeness, we consider two scenarios, the $SU(2)_L$ doublet and the singlet VLLs. Due to their vector-like nature, they escape constraints from the fourth generation searches [9], while non-vanishing couplings to the SM can induce contributions not only to the muon $(g-2)_\mu$ anomaly, but also opening tightly constrained channels such as $\mu \rightarrow e\gamma$ [10].

This article is organized as follows. In Sec. II, we introduce the simplified models, presenting the relevant theoretical details that will serve as the basis behind the subsequent numerical simulations. In Sec. III we introduce the numerical methodology for the studies we conduct in this work. In particular, in Sec. III A, we discuss the implications that additional VLLs have in addressing the $(g-2)_\mu$ anomaly, while in Sec. III B we delve into collider analysis, both in the context of the LHC and future electron (linear) or muon colliders. Finally, in Sec. IV we present our main results and conclude in Sec. V.

II. THE MODELS

In this article, we study collider phenomenology of both $SU(2)_L$ doublet and singlet VLL extensions of the SM accompanied with new right-handed neutrinos. We present the NP and SM fields' quantum numbers in Tabs. I and II respectively.

Field	$SU(3)_C$	$SU(2)_L$	$U(1)_Y$
$E_{L,R}$	1	2	$1/2$
$\mathcal{E}_{L,R}$	1	1	1
ν_R	1	1	0

Table I: Quantum numbers of the new exotic fermions. We adopt the notation of $E_{L,R}$ being an $SU(2)$ doublet, while $\mathcal{E}_{L,R}$ is a singlet, and ν_R is the new right-handed neutrino.

Field	SU(3) _C	SU(2) _L	U(1) _Y	# of generations
Q_L	3	2	1/6	3
L	1	2	-1/2	3
d_R	3	1	-1/3	3
u_R	3	1	2/3	3
e_R	1	1	-1	3
ϕ	1	2	1/2	1

Table II: Quantum numbers for the SM fields. Here, Q_L , d_R , u_R are the quark fields, L and e_R are the lepton fields, and ϕ is the Higgs doublet.

The SU(2)_L doublets are defined as

$$Q_L^i = \begin{bmatrix} u_L \\ d_L \end{bmatrix}^i, \quad L^i = \begin{bmatrix} \nu_L \\ e_L \end{bmatrix}^i, \quad E_{L,R} = \begin{bmatrix} \nu'_{L,R} \\ e'_{L,R} \end{bmatrix}, \quad \phi = \begin{bmatrix} \phi^+ \\ \phi^0 \end{bmatrix}, \quad (1)$$

where i is a generation index, $i = 1, 2, 3$. The most general and renormalizable Lagrangian density of the doublet VLL model, consistent with the symmetries in Tab. I, reads as

$$\begin{aligned} \mathcal{L}_d = & \left(\Theta_i \bar{E}_L e_R^i \phi + \Upsilon \bar{E}_L \nu_R \tilde{\phi} + \Sigma_i \bar{L}^i \nu_R \tilde{\phi} + \Omega \bar{E}_R \nu_R \tilde{\phi} + \Pi_{ij} \bar{L}^i e_R^j \phi + \text{H.c.} \right) + \\ & + M_E \bar{E}_L E_R + M_{LE}^i \bar{L}_i E_R + \frac{1}{2} M_{\nu_R} \bar{\nu}_R \nu_R, \end{aligned} \quad (2)$$

where the Yukawa couplings are denoted by Θ , Υ , Σ , Ω and Π , whereas bi-linear mass terms are indicated by M_E , M_{LE} and M_{ν_R} . For the singlet VLL case, the Lagrangian is written as

$$\mathcal{L}_s = \left(\theta_i \bar{L}^i \mathcal{E}_R \phi + \sigma^i \bar{L}_i \nu_R \tilde{\phi} + \pi_{ij} \bar{L}^i e_R^j \phi + \text{H.c.} \right) + M_E \bar{\mathcal{E}}_L \mathcal{E}_R + \frac{1}{2} M_{\nu_R} \bar{\nu}_R \nu_R, \quad (3)$$

where π , σ and θ are the corresponding Yukawa couplings. The mass matrices for both the singlet and the doublet scenarios, expressed in the $\{e_L^1, e_L^2, e_L^3, e_L'\} \otimes \{e_R^1, e_R^2, e_R^3, e_R'\}$ basis, take the following form

$$M_L^{\text{doublet}} = \begin{bmatrix} \left(\frac{v\Pi}{\sqrt{2}} \right)_{3 \times 3} & (M_{LE})_{3 \times 1} \\ \left(\frac{v\Theta}{\sqrt{2}} \right)_{1 \times 3} & (M_E)_{1 \times 1} \end{bmatrix}, \quad M_L^{\text{singlet}} = \begin{bmatrix} \left(\frac{v\pi}{\sqrt{2}} \right)_{3 \times 3} & \left(\frac{v\theta}{\sqrt{2}} \right)_{3 \times 1} \\ (0)_{1 \times 3} & (M_E)_{1 \times 1} \end{bmatrix}, \quad (4)$$

with $v = 246$ GeV the electroweak symmetry breaking (EWSB) Higgs doublet VEV $(0, v)^\top$, and whose eigenstates describe both the chiral SM-like charged leptons as well as the new VLLs.

For the neutrino sector the mass matrices can be expressed as

$$M_\nu^{\text{doublet}} = \begin{bmatrix} (0_{4 \times 4}) & (M_{LE})_{3 \times 1} \begin{pmatrix} \frac{\Sigma v}{\sqrt{2}} \\ \frac{\Upsilon v}{\sqrt{2}} \end{pmatrix}_{3 \times 1} \\ (M_{LE})_{1 \times 3} & (M_E)_{1 \times 1} \begin{pmatrix} \frac{\Omega v}{\sqrt{2}} \\ \frac{\Omega v}{\sqrt{2}} \end{pmatrix}_{1 \times 1} \\ \begin{pmatrix} \frac{\Sigma v}{\sqrt{2}} \\ \frac{\Upsilon v}{\sqrt{2}} \end{pmatrix}_{1 \times 3} & \begin{pmatrix} \frac{\Upsilon v}{\sqrt{2}} \\ \frac{\Omega v}{\sqrt{2}} \end{pmatrix}_{1 \times 1} & M_{\nu_R} \end{bmatrix}, \quad M_\nu^{\text{singlet}} = \begin{bmatrix} (0)_{3 \times 3} & \left(\frac{\sigma v}{\sqrt{2}} \right)_{3 \times 1} \\ \left(\frac{\sigma v}{\sqrt{2}} \right)_{1 \times 3}^\dagger & (M_{\nu_R})_{1 \times 1} \end{bmatrix}. \quad (5)$$

where the $\{\nu_L^1, \nu_L^2, \nu_L^3, \nu_L', \nu_R, \nu_R\} \otimes \{\nu_L^1, \nu_L^2, \nu_L^3, \nu_L', \nu_R, \nu_R\}$ basis was used for the doublet scenario whereas that of the singlet model was chosen as $\{\nu_L^1, \nu_L^2, \nu_L^3, \nu_R\} \otimes \{\nu_L^1, \nu_L^2, \nu_L^3, \nu_R\}$.

In this article, one considers that the lightest beyond-the-SM (BSM) neutrino is in the keV range and sterile, acting as missing energy in the detector. Therefore, while the neutrino mass matrices above have the standard type-I seesaw form, such a light sterile neutrino implies that M_{ν_R} is equally small, which means that Σ , Υ and Ω (for the doublet scenario) as well as σ (for the singlet scenario), need to be very small in order for both models to be consistent with the active neutrinos mass scale. While a detailed discussion for the neutrino mass generation mechanism is beyond

the scope of this article, it is not a difficult task to minimally extend both the doublet and singlet scenarios, e.g. by introducing the dimension-five Weinberg operator, without affecting our analysis and conclusions [11]. However, the fact that Σ , Υ , Ω and σ need to be very small is calling for the introduction of an approximate global lepton number symmetry, which, for convenience, we define as $U(1)_e \times U(1)_\mu \times U(1)_\tau$, such that only leptons transform non-trivially according to the following quantum numbers:

Field	$U(1)_e$	$U(1)_\mu$	$U(1)_\tau$
$E_{L,R}$	0	1	0
$\mathcal{E}_{L,R}$	0	1	0
ν_R	0	0	0
L^1	1	0	0
L^2	0	1	0
L^3	0	0	1
e_R^1	1	0	0
e_R^2	0	1	0
e_R^3	0	0	1

Table III: Quantum numbers under the approximate lepton number symmetry.

Such an approximate symmetry constrains the model parameters as follows:

- Σ , Υ , Ω (for the doublet case) and σ (for the singlet case) must be tiny in consistency with the smallness of the active neutrino masses;
- the charged lepton-sector Yukawa couplings Π (for the doublet model) and π (for the singlet model), are approximately diagonal and off-diagonal elements can be ignored in our analysis;
- The VLLs solely couple to muons such that only Θ_2 , $M_{LE,2}$ (for the doublet scenario) and θ_2 (singlet scenario) are sizeable and relevant for our numerical studies.

In what follows, we are essentially interested in lepton couplings to both gauge and Higgs bosons. In particular, the focus is on the $W\nu E(\mathcal{E})$, $Z^0 E(\mathcal{E})\ell$ and $HE(\mathcal{E})\ell$ vertices. All numerical computations are performed in the mass basis such that one needs to rotate the gauge eigenstates via the bi-unitary transformations

$$\begin{aligned} \text{Leptons : } M_L^{\text{diag}} &= (U_L^e)^\dagger M_L (U_R^e), \\ \text{Neutrinos : } M_\nu^{\text{diag}} &= (U_\nu)^\dagger M_\nu (U_\nu). \end{aligned} \tag{6}$$

The list of all Feynman rules that are relevant to the numerical analysis are shown in Appendix A.

Before presenting the methodology behind the numerical calculations, it is instructive to revisit the main experimental constraints for VLLs as well as the most relevant couplings for this discussion. First, let us recall that there are not many direct searches for VLLs. In fact, LEP searches have lead to a lower bound on the VLLs mass of $M_{\text{VLL}} > 100.6$ GeV [12], while the most restrictive constraints are coming from CMS where direct searches for doublet VLLs with sizeable couplings to taus are excluded at 95% Confidence Level (CL) in the 120-790 GeV mass range [13]. However, for the model under consideration, the $[U(1)]^3$ lepton number symmetry dictates that the relevant couplings are those to muons such that only the LEP bound applies.

The left-mixing matrix that rotates from the flavour to the mass basis can be parametrized by a single mixing angle, α , as follows

$$U_L^e = \begin{bmatrix} 1 & 0 & 0 & 0 \\ 0 & \cos \alpha & 0 & -\sin \alpha \\ 0 & 0 & 1 & 0 \\ 0 & -\sin \alpha & 0 & -\cos \alpha \end{bmatrix}. \tag{7}$$

With the $U(1)_e \times U(1)_\mu \times U(1)_\tau$ approximate symmetry the mass matrices for both the doublet and singlet cases take

a simple form

$$M_L^{\text{doublet}} = \begin{bmatrix} \frac{v\Pi_{11}}{\sqrt{2}} & 0 & 0 & 0 \\ 0 & \frac{v\Pi_{22}}{\sqrt{2}} & 0 & M_{LE,2} \\ 0 & 0 & \frac{v\Pi_{33}}{\sqrt{2}} & 0 \\ 0 & \frac{v\Theta_2}{\sqrt{2}} & 0 & M_E \end{bmatrix}, \quad M_L^{\text{singlet}} = \begin{bmatrix} \frac{v\Pi_{11}}{\sqrt{2}} & 0 & 0 & 0 \\ 0 & \frac{v\Pi_{22}}{\sqrt{2}} & 0 & \frac{v\theta_2}{\sqrt{2}} \\ 0 & 0 & \frac{v\Pi_{33}}{\sqrt{2}} & 0 \\ 0 & 0 & 0 & M_E \end{bmatrix}. \quad (8)$$

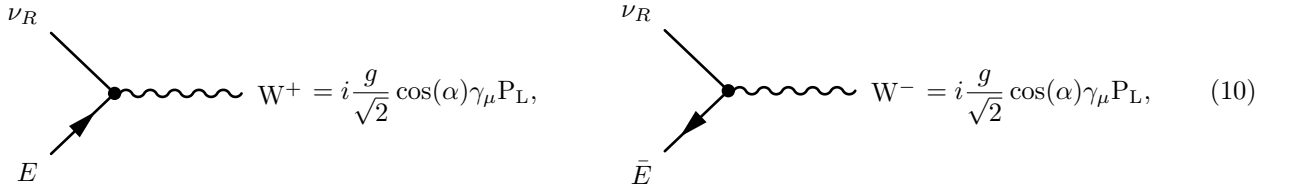
Besides lepton mixing terms one also considers a neutrino mixing with the following structure,

$$U_\nu^{\text{doublet}} = \begin{bmatrix} (U_{\text{PMNS}})_{11} & (U_{\text{PMNS}})_{12} & (U_{\text{PMNS}})_{13} & 0 & 0 & 0 \\ (U_{\text{PMNS}})_{21} & (U_{\text{PMNS}})_{22} & (U_{\text{PMNS}})_{23} & 0 & 0 & 0 \\ (U_{\text{PMNS}})_{31} & (U_{\text{PMNS}})_{32} & (U_{\text{PMNS}})_{33} & 0 & 0 & 0 \\ 0 & 0 & 0 & 1 & 0 & 0 \\ 0 & 0 & 0 & 0 & (U_\nu)_{55} & (U_\nu)_{56} \\ 0 & 0 & 0 & 0 & (U_\nu)_{65} & (U_\nu)_{66} \end{bmatrix}, \quad (9)$$

$$U_\nu^{\text{singlet}} = \begin{bmatrix} (U_{\text{PMNS}})_{11} & (U_{\text{PMNS}})_{12} & (U_{\text{PMNS}})_{13} & 0 \\ (U_{\text{PMNS}})_{21} & (U_{\text{PMNS}})_{22} & (U_{\text{PMNS}})_{23} & 0 \\ (U_{\text{PMNS}})_{31} & (U_{\text{PMNS}})_{32} & (U_{\text{PMNS}})_{33} & 0 \\ 0 & 0 & 0 & 1 \end{bmatrix}$$

where the 3×3 SM block is fixed by the Pontecorvo–Maki–Nakagawa–Sakata (PMNS) matrix [14]. Technically, and considering only such a block, the PMNS matrix must in rigour be defined as $U_{\text{PMNS}} = U_\nu \cdot U_L^\dagger$ such that the actual mixing is instead given as $(U_{\text{PMNS}})_{i1} = (U_\nu)_{i1}$, $(U_{\text{PMNS}})_{i3} = (U_\nu)_{i3}$ and $(U_{\text{PMNS}})_{i2} = (U_\nu)_{i2} \cos \alpha$ with $i = 1, 2, 3$. However, the benchmark scenarios considered in Sec. IV are such that $\cos \alpha \approx 1$ for both the doublet and the singlet models and therefore the parametrization in Eq. (9) is consistent with a realistic lepton mixing.

The 2×2 block in the doublet case represents the mixing between the ν_5 and ν_6 mass eigenstates. These elements do not contribute to the interaction vertices used in our analysis and therefore their size and numerical values are not relevant for the discussion. For consistency, we assume a generic $\mathcal{O}(1)$ mixing. It also follows from the approximate lepton number symmetry that the mixing between the right-handed neutrino and the remaining neutral leptons is negligible and can be ignored. This means that $(U_\nu)_{44} = 1$, $(U_\nu)_{4j} = (U_\nu)_{j4} = 0$ and the couplings between the SM and BSM neutrinos can be neglected, thus maximizing the strength of the $W\nu_R E(\mathcal{E})$ interaction vertex. Focusing on the doublet model first, the Feynman rules for such a vertex read as



$$\begin{array}{c} \nu_R \\ \swarrow \\ \bullet \\ \nearrow E \end{array} \text{---} W^+ = i \frac{g}{\sqrt{2}} \cos(\alpha) \gamma_\mu P_L, \quad \begin{array}{c} \nu_R \\ \swarrow \\ \bullet \\ \nearrow \bar{E} \end{array} \text{---} W^- = i \frac{g}{\sqrt{2}} \cos(\alpha) \gamma_\mu P_L, \quad (10)$$

where, in the limit of $\alpha \rightarrow 0$, one recovers a pure gauge interaction. Furthermore, consistency with the muon $(g-2)_\mu$ measurement requires the cosine of the mixing angle α to be smaller but not far from unity. With such a small mixing, lepton flavour violation observables can be kept under control and the VLL single production cross-section is dominated by the $W\nu_R E$ vertex as we discuss in Sec. III B. For the singlet model, on the other hand, it follows from the approximate lepton number symmetry that the smallness of the σ Yukawa coupling results in a negligible $W\nu_R \mathcal{E}$ interaction strength. Therefore, in our numerical analysis, one can ignore such interactions by safely setting it to zero.

Another important element to take into consideration is the VLL decay width. In particular, for the considered scenario, where $M_{E,\mathcal{E}} \gg m_{\nu_R}$, it can be expressed as

$$\Gamma(E(\mathcal{E}) \rightarrow W\nu_R) = \frac{g^2 U_{\text{MIX}}^2 m_{E,\mathcal{E}}^2}{64\pi M_W^2} \left(1 - \frac{M_W^2}{m_{E,\mathcal{E}}^2}\right)^2 \left(1 + 2 \frac{M_W^2}{m_{E,\mathcal{E}}^2}\right). \quad (11)$$

Here, $U_{\text{MIX}}^2 = \cos^2 \alpha$ for the doublet model while for the singlet case it vanishes. One notes that such a decay width grows as a power law in m_E , becoming rather significant for large masses as shown in Fig. 1. For example, taking the

case where $U_{\text{MIX}} = 1$, one can observe that for a mass of 2 TeV, the decay width already surpasses the mass itself with $\Gamma = 2705.4$ GeV. While such an effect can be mitigated for larger mixing angles as demonstrated in Fig. 1, if U_{MIX} deviates too much from unity the PMNS matrix also becomes unrealistic. This means that we are phenomenologically bounded to the small mixing regime where U_{MIX} is not too far from 1. However, a decay width greater than its mass leads to conceptual issues with respect to the interpretation of such large-width fields as particles. In fact, within the context of Quantum Field Theory, a large value for the width implies that the particle is highly non-local and the narrow-width approximation is no longer valid calling for a more robust framework to describe it (see e.g. [15–17]). In this article, we avoid such a scenario and require a mass range where the width of the doublet VLL is always lower than its mass. Although the widths must be kept under control, a sizeable value has interesting experimental implications. For instance, it results in wider distributions of kinematic variables such as the mass and the transverse momentum (p_T), where large tails can extend into phase space regions not populated by the SM background events.

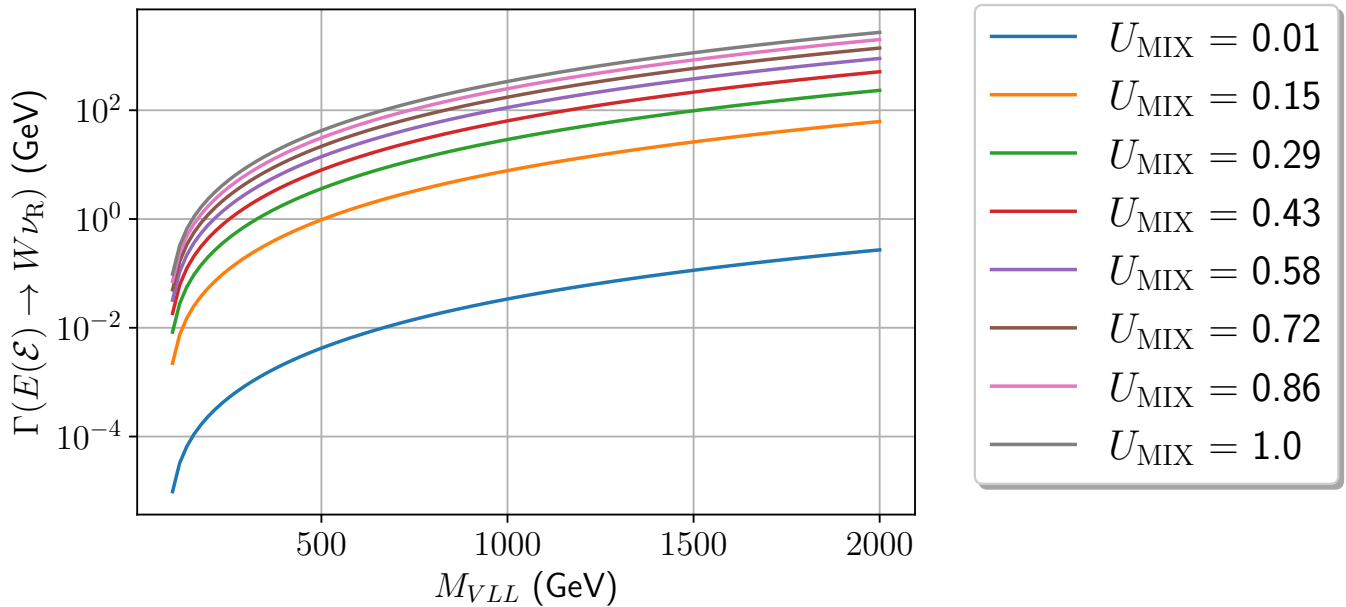


Figure 1: Decay width as a function of the VLL’s mass, both displayed in GeV. Each coloured line is representative of a different mixing element, whose numerical value is displayed in the box to the right of the plot.

III. VLLS: COLLIDER PHENOMENOLOGY AND $(g - 2)_\mu$

A. Anomalous magnetic moment of the muon

Current measurements of the anomalous magnetic moment of the muon (a_μ^{exp}) indicate a tension of 4.2 standard deviations from the SM prediction (a_μ^{SM}) [3],

$$\Delta a_\mu = a_\mu^{\text{exp}} - a_\mu^{\text{SM}} = 251(59) \times 10^{-11}, \quad (12)$$

where the total uncertainty is shown in parenthesis. Within the SM, the dominant contribution to the theoretical uncertainty comes from hadronic vacuum polarization (HVP), intrinsically related to loop corrections to which any new particle with direct or indirect couplings to the muons can potentially provide relevant contributions. As discussed in Sec. II, the approximate lepton number symmetry dictates that the VLLs only couple to muons and can therefore generate non-negligible contributions to its anomalous magnetic moment. These contributions arise in the form of one-loop corrections to Δa_μ where VLLs propagators are either accompanied by Z^0 or Higgs bosons. We define the

total VLL contribution as follows

$$\Delta a_\mu^{\text{VLL}} = \begin{array}{c} \gamma \\ \text{---} \\ \bullet \\ \text{---} \bar{E}/\bar{\varepsilon} \quad E/\varepsilon \\ \text{---} \bullet \quad \text{---} \bullet \\ \text{---} \mu^- \quad \text{---} \mu^- \\ \text{---} H \end{array} + \begin{array}{c} \gamma \\ \text{---} \\ \bullet \\ \text{---} \bar{E}/\bar{\varepsilon} \quad E/\varepsilon \\ \text{---} \bullet \quad \text{---} \bullet \\ \text{---} \mu^- \quad \text{---} \mu^- \\ \text{---} Z^0 \end{array} . \quad (13)$$

Generic formulae for $\Delta a_\mu^{\text{VLL}}$ in this form are well known in the literature [18–21]. The details of the calculation of the loop integrals can be found in [22]. For instance, the Z^0 -boson contribution to the anomaly is given by

$$\Delta a_\mu^{Z^0} = -\frac{m_\mu}{8\pi^2 M_{Z^0}^2} \left[m_\mu \left(|g_R^Z|^2 + |g_L^Z|^2 \right) F_{Z^0}(x_{Z^0}) - M_{\text{VLL}} \text{Re}\{g_R^Z g_L^{Z*}\} G_{Z^0}(x_{Z^0}) \right], \quad (14)$$

where $x_{Z^0} = (M_{\text{VLL}}/M_{Z^0})^2$ and the loop functions F_{Z^0} and G_{Z^0} are defined as

$$F_{Z^0}(x) = \frac{5x^4 - 14x^3 + 39x^2 - 38x + 8 - 18x^2 \ln x}{12(1-x)^4}, \quad (15)$$

$$G_{Z^0}(x) = \frac{-x^3 - 3x + 4 + 6x \ln x}{2(1-x)^3}.$$

The second contribution contains a Higgs boson propagator in the loop and reads as

$$\Delta a_\mu^H = \frac{m_\mu}{32\pi^2 M_H^2} \left[m_\mu \left(|g_R^H|^2 + |g_L^H|^2 \right) F_H(x_H) + M_{\text{VLL}} \text{Re}\{g_R^H g_L^H\} G_H(x_H) \right], \quad (16)$$

where, once again, one denotes $x_H = (M_{\text{VLL}}/M_H)^2$ and the loop functions are given by

$$F_H(x) = \frac{x^3 - 6x^2 + 3x + 2 + 6x \ln x}{6(1-x)^4}, \quad (17)$$

$$G_H(x) = \frac{-x^2 + 4x - 3 - 2 \ln x}{(1-x)^3}.$$

The left- and right-handed projections of the VLL couplings to the Z^0 ($g_{L,R}^Z$) and Higgs bosons ($g_{L,R}^H$), can be read from the Feynman rules corresponding to the diagrams (A1) to (A8). For the numerical analysis of the $(g-2)_\mu$ we consider the same mixing as shown in Eq. (7). Note that the approximate $[\text{U}(1)]^3$ lepton number symmetry has interesting implications in the couplings with the Z^0 boson. Namely, it implies that the left-handed coupling for the doublet case is identically zero, while for the singlet scenario the right-handed coupling is the one that vanishes. To see this, let us inspect the doublet case. In this instance, the left-handed coupling is given by the Feynman rule in Eq. (A1). Replacing various mixing elements with the ones indicated in Eq. (7), we have

$$g_L^Z = \frac{1}{2}(g \cos \theta_W - g' \sin \theta_W) \left[(U_L^\varepsilon)_{44}^* (U_L^\varepsilon)_{24} + \sum_{a=1}^3 (U_L^\varepsilon)_{4a}^* (U_L^\varepsilon)_{2a} \right] \Leftrightarrow$$

$$\Leftrightarrow g_L^Z = \frac{1}{2}(g \cos \theta_W - g' \sin \theta_W) [\cos \alpha \sin \alpha - \sin \alpha \cos \alpha] \Leftrightarrow g_L^Z = 0. \quad (18)$$

For such a cancellation not to occur one needs to consider charge-parity violation in the leptonic sector, that is, a complex mixing matrix, as opposed to an orthogonal one. Analogous calculations show that for the singlet model, the right-handed coupling is the one that goes to zero. The same effect does not take place in VLL couplings to muons and Higgs bosons. Taking the above into account, the $(g-2)_\mu$ expressions for the Z^0 contributions can be simplified and expressed as

$$\text{Doublet : } \Delta a_\mu^{Z^0} = -\frac{m_\mu^2 |g_R^Z|^2}{8\pi^2 M_{Z^0}^2} F_{Z^0} \left(\frac{M_{\text{VLL}}^2}{M_{Z^0}^2} \right), \quad (19)$$

$$\text{Singlet : } \Delta a_\mu^{Z^0} = -\frac{m_\mu^2 |g_L^Z|^2}{8\pi^2 M_{Z^0}^2} F_{Z^0} \left(\frac{M_{\text{VLL}}^2}{M_{Z^0}^2} \right).$$

One can then observe that the Z^0 contribution is always negative since all loop functions are positive for $x_{Z^0} > 0$. As such, one needs to strongly rely on the Higgs channel in order to potentially explain Δa_μ in the context of the model under consideration. In particular, and noting that the second term in Eq. (16) is proportional to the mass of the VLL, it will offer the dominant contribution to Δa_μ^H . We can then approximate the Higgs channel correction to $(g - 2)_\mu$ as

$$\Delta a_\mu^H \sim \frac{m_\mu M_{\text{VLL}}}{32\pi^2 M_H^2} \text{Re}\{g_R^H g_L^H\} G_H(x_H). \quad (20)$$

It is important to note that the non-zero mixing elements between the VLLs and the muon can trigger Lepton Flavour Violation (LFV) interactions. Therefore it is important to confront all points considered in our numerical analysis with the following LFV branching ratios (BR): $\text{BR}(\mu \rightarrow e\gamma)$, $\text{BR}(\tau \rightarrow e\gamma)$, $\text{BR}(\tau \rightarrow \mu\gamma)$, $\text{BR}(\mu^- \rightarrow e^- e^+ e^-)$, $\text{BR}(\tau^- \rightarrow e^- e^+ e^-)$, $\text{BR}(\tau^- \rightarrow \mu^- \mu^+ \mu^-)$, $\text{BR}(\tau^- \rightarrow e^- \mu^+ \mu^-)$, $\text{BR}(\tau^- \rightarrow \mu^- e^+ e^-)$, $\text{BR}(\tau^- \rightarrow \mu^- e^+ \mu^-)$, $\text{BR}(\tau^- \rightarrow e^- \mu^+ e^-)$, $\text{BR}(\tau^+ \rightarrow \pi^0 e^+)$ and $\text{BR}(\tau^+ \rightarrow \pi^0 \mu^+)$. For such a purpose we use the latest version of **SPheno** [23] to generate the Wilson coefficient cards, which are then passed to **flavio** [24] in order to compute the corresponding LFV observables. It is important to mention that **SPheno** also computes the BRs i.e. **flavio** merely works as an extra layer of added scrutiny, even if both programs' numerical outputs (for the BRs) are well within each other's error and are therefore compatible. We use the 90% CL experimental limits on the considered LFV observables as reported in the most recent issue of the PDG review [10].

B. Collider analysis: LHC and muon colliders

The analysis techniques and Deep Learning algorithms used in the current study for both the doublet and the singlet models were first implemented in [25] and [26], respectively. Starting with the doublet case, the channel we are probing is characterised by a final state with one isolated charged lepton from the W boson decay, and missing energy (MET) associated with the undetected neutrinos. In particular, we consider the channel where the charged lepton is a muon. At Leading Order (LO), the production diagram, at the LHC, can be seen in Fig. 2. For this signal topology, we consider the irreducible background together with all physics processes that lead to the production of, at least, one muon and up to two jets in the final state, $pp \rightarrow \mu^- \bar{\nu}_\mu$ (+jets). In the case of the VLL doublet, two diagrams contribute for the signal, one with the right-handed neutrino and another one with a muonic neutrino. For the singlet production only, the diagram with the muonic neutrino contributes to the cross section. This can be seen from the Feynman rules in Eqs. (A2) and (A3) for the doublet case and in Eqs. (A6) and (A7) for the singlet scenario where the strength of the interaction vertex is controlled by the extended PMNS matrix. For instance, and noting that only the left chirality projection of the couplings are non-zero, we have

$$g_L^{E\nu_\mu W} = \frac{g}{\sqrt{2}} \sin \alpha [U_\nu^{\text{doublet}}]_{22}, \quad g_L^{E\nu_R W} = \frac{g}{\sqrt{2}} \cos \alpha, \quad g_L^{\mathcal{E}\nu_\mu W} = \frac{g}{\sqrt{2}} \sin \alpha [U_\nu^{\text{singlet}}]_{22}. \quad (21)$$

This in turn means that the cross section for the doublet case will be much larger than the one for the singlet case, because the strength of the dominant contribution for the former, in particular the coupling to right-handed neutrinos, is proportional to $\cos \alpha$ while for the latter it is controlled by $\sin \alpha$.

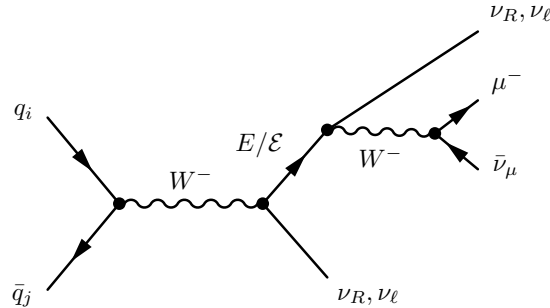


Figure 2: LO Feynman diagram for VLL single production. q_i and \bar{q}_j correspond to quarks originating from the initial protons, ν_R is the right-handed neutrino and ν_ℓ are the SM neutrinos.

The analysis follows a well-defined guideline. Both models are first implemented in **SARAH** [27] to generate all interaction vertices as well as all relevant files that interface with Monte-Carlo generators, namely, **MadGraph5** [28] for

quark-level matrix-element calculations and **Pythia8** [29] for hadronization and showering leading to final state particles. In **MadGraph5** we simulate proton-proton collisions at a centre-of-mass energy $\sqrt{s} = 14$ TeV, for a total of 250k events for the signal and backgrounds. We also employ the default LO parton-distribution function NNPDF2.3 [30] which fixes the evolution of the strong coupling constant, α_s . Fast-simulation of the ATLAS detector is conducted, with **Delphes** [31]. All kinematic distributions are extracted with the help of **ROOT** [32]. At this stage, we also impose selection criteria, to maximise the signal significance. In particular, all events must satisfy

$$\begin{aligned} p_T(\mu^-) &> 25 \text{ GeV}, \\ \text{MET} &> 15 \text{ GeV and} \\ |\eta(\mu^-)| &\leq 2.5, \end{aligned}$$

where η represents the muon pseudo-rapidity¹. Note that the signal production represented in Fig. 2, is characterized by having no jets in the final states. While it is true that the lack of no jet candidates at any given event in a hadron collider is perhaps too unrealistic, the absence of such selection can also cause complications in the Deep Learning algorithms used later in the analysis, since signal/background classes are incredibly unbalanced and may lead to over-fitting problems. The kinematics of final states for both signal and background events are translated into

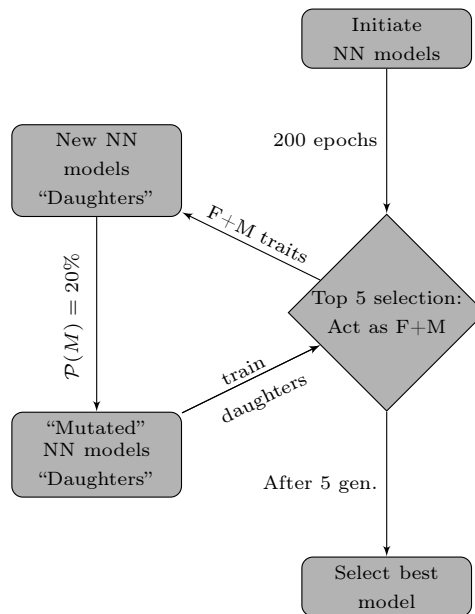


Figure 3: Flowchart representative of all iterative steps involved in the genetic algorithm that we employ in this work.

tabular datasets and used as inputs for neural models, whose job is to separate the signal from the background. The neural network is constructed using **Keras** [33]. For classification, we choose a set of 9 observables computed in the laboratory frame. Low-level features include the muon observables $\cos(\theta_{\mu^-})$, $\eta(\mu^-)$, $\phi(\mu^-)$ and $p_T(\mu^-)$ as well as the MET. Some reconstructed variables are also considered, which include $M_T(W^-)$, $\eta(W^-)$ and $p_T(W^-)$, corresponding to the W boson transverse mass, eta and transverse momentum, respectively².

To optimize the neural network architecture, we employ a genetic algorithm following the same steps as described in [25, 26] and schematically represented in the diagram of Fig. 3. The algorithm begins by first generating an arbitrary number of neural networks, whose architecture is determined by randomly pooling a list of predefined hyperparameters (number of layers, activation functions, regularisers, etc.). We then train each individual network over the data for a given number of epochs. From the trained networks, we pick the top five best performing ones. From these, we create Father-Mother pairs, where we combine 50% of the Father's traits (that is, its hyperparameters) and 50% of the Mother traits to construct new neural architectures, which we dub as Daughters. We also consider the possibility

¹ The pseudorapidity of a particle is defined as $\eta = -\ln(\tan(\theta/2))$, where θ is its polar angle.

² The transverse mass, in the limit of massless final particles, is $M_T^2 = 2p_{T,1}p_{T,2}[1 - \cos(\theta_{1,2})]$, where 1 and 2 are labels for the two final state particles.

of mutation, that is, after the Daughter networks have been built, we consider that the hyperparameters may change to another, with the probability of $\mathcal{P}(M) = 20\%$. We then train the Daughter networks for a given number of epochs and repeat the procedure for a set of generations. Finally, we select the best performing network based on some metric of choice. In our analysis, the algorithm is designed to maximise the Asimov statistical significance, defined as

$$\mathcal{Z}_A = \left[2 \left((s+b) \ln \left(\frac{(s+b)(b+\sigma_b^2)}{b^2 + (s+b)\sigma_b^2} \right) - \frac{b^2}{\sigma_b^2} \ln \left(1 + \frac{\sigma_b^2 s}{b(b+\sigma_b)} \right) \right) \right]^{1/2}. \quad (22)$$

With the LHC being a proton collider, production of coloured particles by the strong interaction is heavily favoured, compared to identical processes involving electroweak bosons. As VLLs are colour singlets, they can only be produced via this last interaction at LO. It is then worth mentioning that, in addition to the obvious motivation of studying VLL production at the LHC already during RUN3 and, later on, in its high luminosity phase (HL-LHC), it is of utmost importance to understand the sensitivity with which these new particles can be probed, at future colliders. In

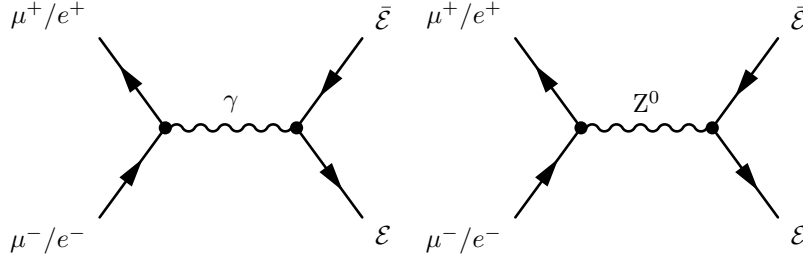


Figure 4: LO Feynman diagrams for VLL double production at a lepton/anti-lepton collider via exchange of either a photon or a Z^0 boson.

particular, there has been an active discussion within the community about e^+e^- colliders like the Compact Linear Collider (CLIC) [34, 35] or the International Linear Collider (ILC) [36], and more recently, on the possibility of building a $\mu^-\mu^+$ collider [37, 38]. Besides offering cleaner environments, when compared to hadronic machines, production via electroweak processes is favoured, hence, VLLs should have a higher chance of being observed, in case they exist, in this type of machines. For this purpose, we perform numerical and analytical computations with **FeynCalc** [39] for the pair-production of VLLs whose tree-level diagrams can be seen in Fig. 4. As previously stated, singlets have lower couplings compared to doublets, hence we discuss the prospects for VLL discovery at lepton colliders for the singlet scenario and not the doublet, as this can be seen as the worst-case scenario. Do note, however, that the conclusions one takes from the singlet model can be easily generalized to the doublet model. That is, the only difference between the collider studies for the two scenarios are the values of the couplings.

In conclusion, the single VLL production is favoured at the LHC for the doublet case, due mainly to the strength of the couplings. Double production of VLLs has the obvious disadvantage of the need to produce two heavy states and a more elaborate final state to detect. If one wants to probe the singlet model, and assuming that it cannot be done at the LHC, the future lepton colliders, where single production is precluded at LO, may give us enough VLLs in the double production channel to test the singlet VLL scenario.

IV. RESULTS

In this section, we present all numerical results for the LHC and for future lepton colliders, while taking into account the possibility of solving the $(g-2)_\mu$ anomaly. In order to get a good handle of the allowed parameter values before choosing the benchmark points used in the collider studies, we start our discussion by looking into the constraints imposed by the muon anomalous magnetic moment measurement.

As discussed before in Section III A, the Z^0 contributions are subleading and negative, while the dominant effects result almost entirely from the loops with a Higgs boson propagator. Taking Eq. (20) into consideration, we can then use this information to constraint the possible values of the product of the left and right chiral Higgs boson couplings, $g_L^H g_R^H$, as a function of the mass of the VLL. We start by showing in Fig. 5 the allowed 1σ (2σ) bands in green (yellow) for the values of the muon anomalous magnetic moment, as a function of the VLL mass. Fig. 5 will become important later on, when discussing the collider results. In Fig. 6 we present the corresponding contour plot that showcases the viable region within the allowed 1σ (2σ) band in green (yellow) in terms of the product of the left and right chirality projections of the $H\mu E(\mathcal{E})$ coupling $g_L^H g_R^H$, as a function of the VLL mass. Both the singlet and the doublet

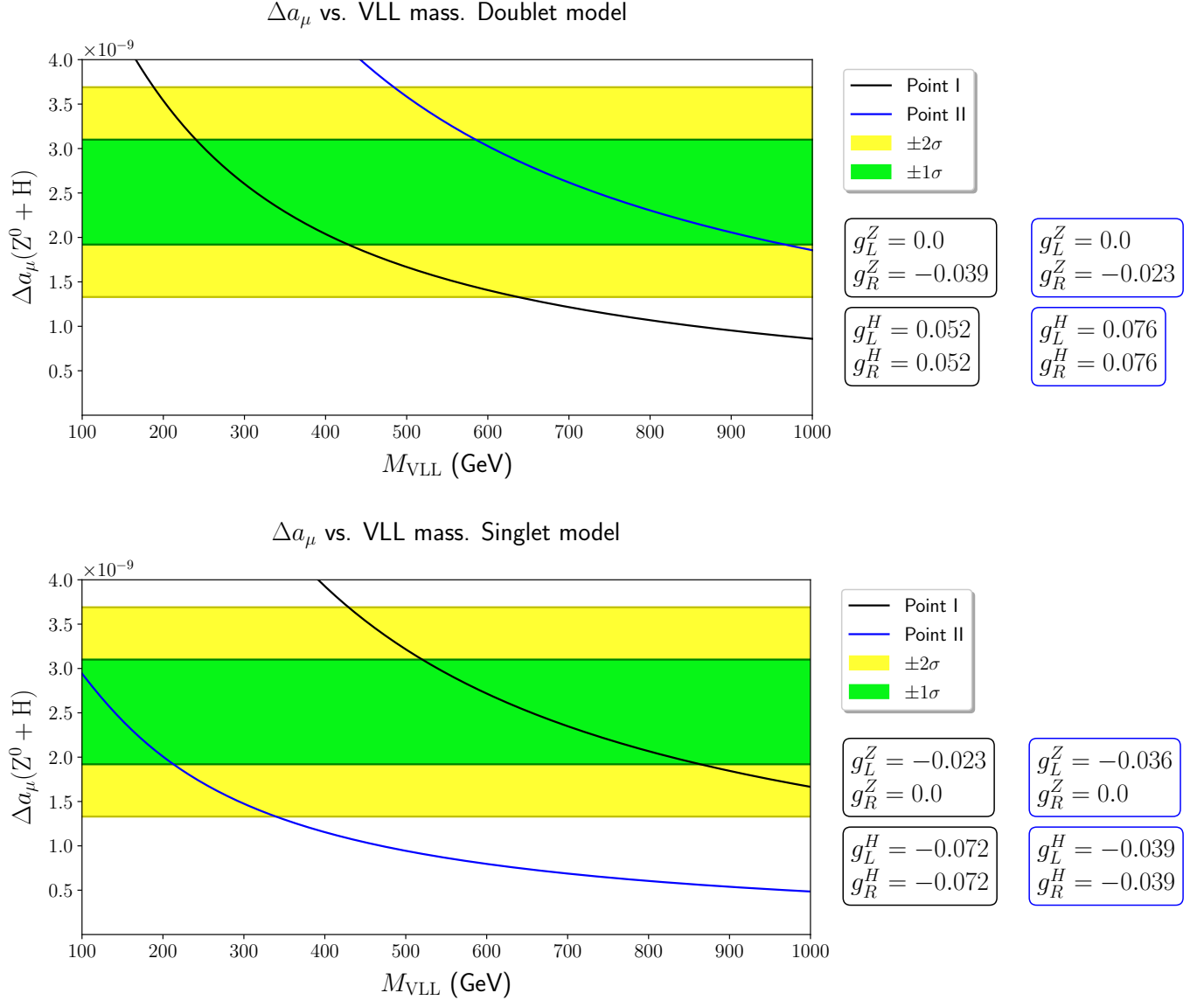


Figure 5: VLL contributions to the anomalous magnetic moment of the muon as a function of the VLL’s mass. Upper and lower 2σ bounds are coloured in yellow, whereas 1σ bounds are shown in green. The black and blue lines are representative of two distinct scenarios, for which the corresponding left and right couplings are given in rectangular boxes to the left side of the plots. In the top panel we present the numerical results for a doublet VLL while in the bottom one we focus on the singlet scenario. For the singlet case we use the blue line as a benchmark scenario for collider studies, in particular, to select the two points at the bottom of Tab. V whereas, for the doublet model, we use the black line when referring to masses up to 500 GeV and the blue line for benchmark points heavier than 600 GeV.

models have identical structures, which is indeed expected since the functional form for the couplings is identical (see the Feynman rules (A4) and (A8) in Appendix A). In particular, one can explain the anomalous magnetic moment of the muon within a 2σ uncertainty band both for a light VLL with mass $M_{\text{VLL}} = 100$ GeV, where $g_L^H g_R^H \in [6.93 \times 10^{-4}, 2.01 \times 10^{-3}]$, as well as for a heavy VLL scenario with $M = 1$ TeV if $g_L^H g_R^H \in [4.14 \times 10^{-3}, 1.15 \times 10^{-2}]$. For completeness, we show in Fig. 7, the allowed mass range to explain Δa_μ provided that $g_{L,R}^H$ remain perturbative, *i.e.* $\max(g_{L,R}^H) = \sqrt{4\pi}$. As one can observe, these simplified models can explain the anomaly up to a mass of 1.2 PeV at the cost of large couplings. In Tab. IV, the numerical values for the blue and black stars in Fig. 5 are shown. Notice that, in agreement with our discussion above, the Z^0 diagram in Eq. (13) clearly plays a sub-leading role in the determination of Δa_μ , typically of order $\mathcal{O}(10^{-11} - 10^{-12})$ and with the opposite sign.

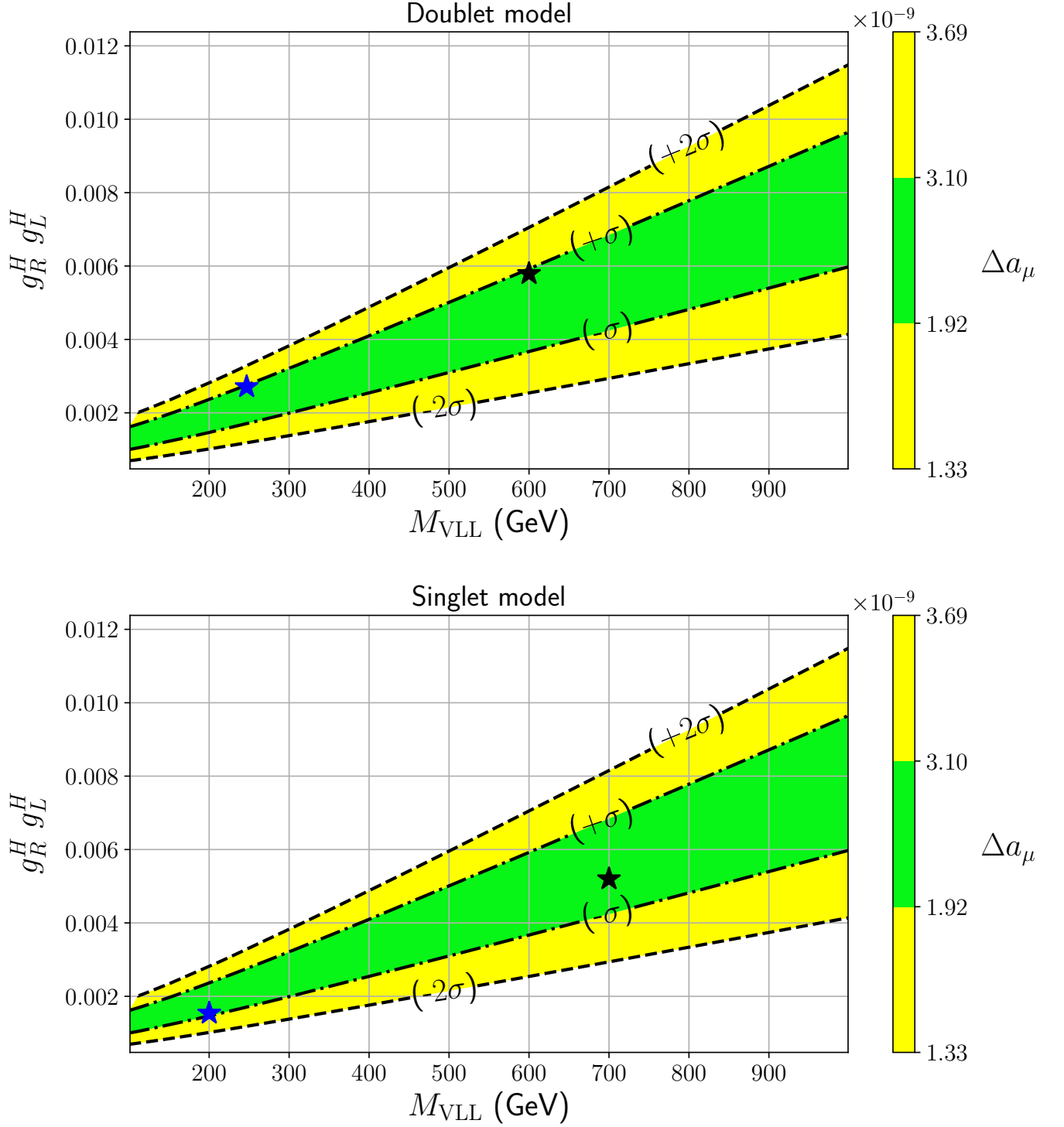


Figure 6: Contour plot for the product of the left and right chirality projections of the Higgs-muon-VLL couplings as a function of the VLL's mass. The top panel represents the doublet model while the bottom one refers to the singlet case. The 1σ uncertainty band is highlighted in green whereas the 2σ band is shown in yellow. The blue and black stars correspond to a particular choice of the VLL mass on the blue and black lines in Fig. 5 respectively, where the current value of Δa_μ is reproduced within 1σ uncertainty. These four points are further shown in Tab. IV. The couplings obtained for both the blue and black scenarios in each model are used in the collider analysis where we only vary the VLL mass.

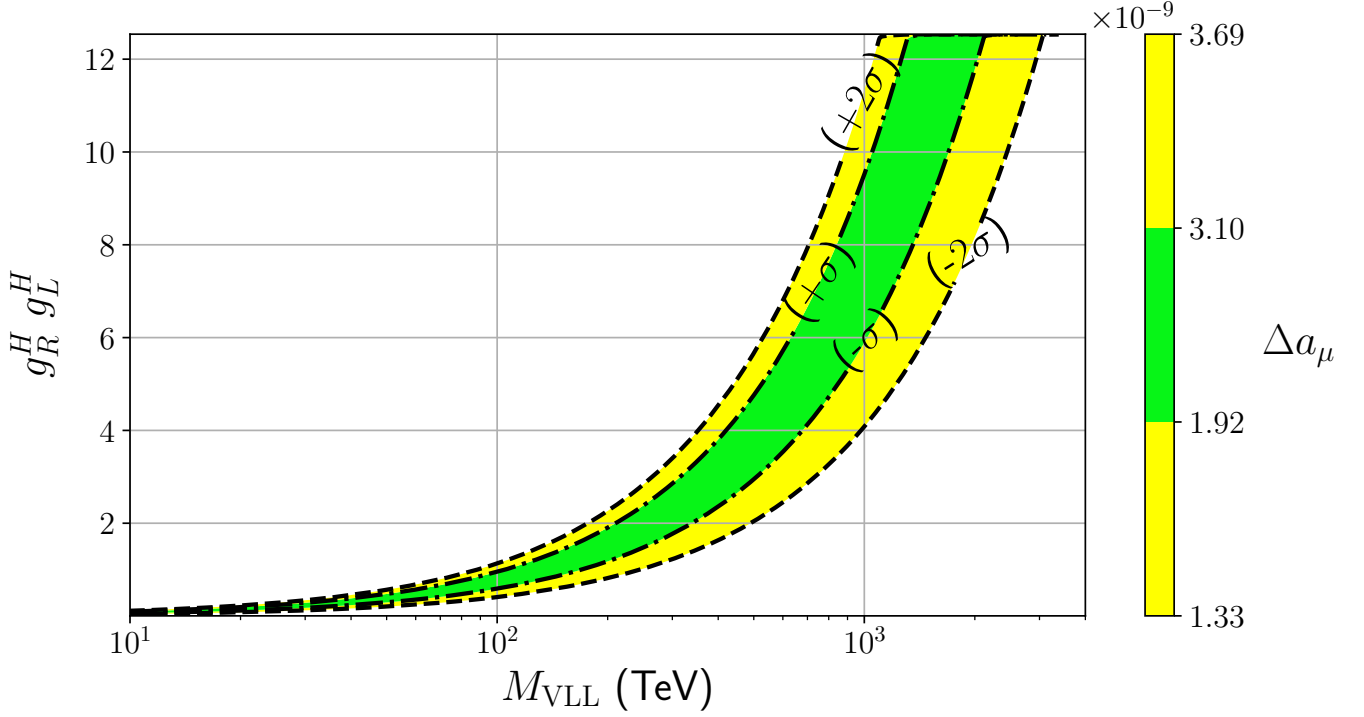


Figure 7: Contour plot of the product of the left- and right-handed Higgs couplings as a function of the VLL’s mass. The 1σ region is plotted in green, whereas the 2σ region is shown in yellow. In the y -axis, we consider couplings until we reach the perturbative limit, that is, $\max(g_L^H) = \max(g_R^H) = \sqrt{4\pi}$. In the x -axis, the mass of the VLL is shown in units of TeV and is present in logarithmic scale.

	$\Delta a_\mu(Z^0)$	$\Delta a_\mu(H)$	$\Delta a_\mu(Z^0) + \Delta a_\mu(H)$	$M_{\text{VLL}} \text{ (GeV)}$	g_L^H	g_R^H	g_L^Z	g_R^Z
Black star	$-1.121275 \times 10^{-11}$	3.046836×10^{-9}	3.035623×10^{-9}	246.89	0.052	0.052	0.0	-0.039
Blue star	$-3.784224 \times 10^{-12}$	3.031409×10^{-9}	3.027625×10^{-9}	600.01	0.076	0.076	0.0	-0.023
Black star	$-3.611453 \times 10^{-12}$	2.352712×10^{-9}	2.349101×10^{-9}	700.00	-0.072	-0.072	-0.023	0.0
Blue star	$-9.999721 \times 10^{-12}$	2.016000×10^{-9}	2.006001×10^{-9}	200.09	-0.039	-0.039	-0.036	0.0

Table IV: Benchmark points for the anomalous magnetic moment shown in Fig. 6. The first two rows are representative of the doublet scenario, whereas the bottom two are indicative of the singlet model.

Let us now focus the discussion on the collider analysis. In Fig. 5, the blue and black lines represent four distinct scenarios (two for each model), where all couplings are fixed and only the VLL mass varies. In order to comply with the muon $(g - 2)_\mu$ anomaly within a 2σ uncertainty or, at least, not too far from it, we select points belonging to the blue and the black lines in the remainder of this article. We first consider a benchmark point where we set the VLL mass to $M_{\text{VLL}} = 700 \text{ GeV}$ and fix the right-handed neutrino mass to $M_{\nu_R} = 200 \text{ keV}$ [25]. In accordance with the $(g - 2)_\mu$ constraints, for the doublet and singlet cases this point corresponds to the blue and black lines of Fig. 5, respectively. It is assumed that the neutrino acts as a DM candidate, thus responsible for missing energy at the detector level. In fact, recent studies [40] constrain a DM neutrino mass to be heavier than 12 keV making our scenarios compatible with such a picture. However, any further details about the dark properties of our sterile neutrinos are beyond the scope of this article. Note also that, according to the studies in [25], variations of the sterile neutrino mass, at least up to 100 MeV, play no role in the discovery/exclusion significance for a fixed VLL mass. The remaining BSM neutrinos present in the doublet model share, at LO, the same mass with their $\text{SU}(2)_L$ doublet VLL counterpart. Contrary to the right-handed neutrinos, these cannot be dark since they efficiently decay into W^\pm bosons and muons according to the Feynman rule

$$g_R^W = -\frac{g}{\sqrt{2}} [U_\nu]_{55} [U_R^e]_{24} , \quad (23)$$

where, for the benchmark points considered in our study, $[U_\nu]_{55} \approx [U_R^e]_{24} \approx 1$. In particular, we fix the mixing matrices in such a way to be compatible with the muon $(g-2)_\mu$ anomaly, which, for the doublet model, read as

$$\begin{aligned}
 U_L^e &= \begin{bmatrix} 1 & 0 & 0 & 0 \\ 0 & 0.9249217 & 0 & -0.02215850 \\ 0 & 0 & 1 & 0 \\ 0 & -0.02215850 & 0 & 0.9997545 \end{bmatrix}, & U_L^e &= \begin{bmatrix} 1 & 0 & 0 & 0 \\ 0 & 0.9970072 & 0 & -0.07730876 \\ 0 & 0 & 1 & 0 \\ 0 & -0.07730876 & 0 & 0.9970072 \end{bmatrix}, \\
 U_R^e &= \begin{bmatrix} 1 & 0 & 0 & 0 \\ 0 & 0.0482131 & 0 & -0.998837 \\ 0 & 0 & 1 & 0 \\ 0 & 0.998837 & 0 & 0.0482131 \end{bmatrix}, & U_R^e &= \begin{bmatrix} 1 & 0 & 0 & 0 \\ 0 & 0.0312138 & 0 & -0.999513 \\ 0 & 0 & 1 & 0 \\ 0 & 0.999513 & 0 & 0.0312138 \end{bmatrix}, \\
 U_\nu &= \begin{bmatrix} U_{\text{PMNS}} & 0 \\ 0 & U_\nu^{\text{BSM}} \end{bmatrix}, & U_\nu^{\text{BSM}} &= \begin{bmatrix} 1 & 0 & 0 \\ 0 & -0.960772 & -0.277338 \\ 0 & 0.277338 & -0.960772 \end{bmatrix}.
 \end{aligned} \tag{24}$$

The blue and black charged lepton mixing matrices correspond to the blue and black stars in the top panel of Fig. 6. The neutrino mixing is identical for both cases and therefore is only shown in black. For the singlet model, the mixing matrices are as follows

$$\begin{aligned}
 U_L^e &= \begin{bmatrix} 1 & 0 & 0 & 0 \\ 0 & 0.99883294 & 0 & -0.0482984918 \\ 0 & 0 & 1 & 0 \\ 0 & -0.0482984918 & 0 & 0.99883294 \end{bmatrix}, & U_L^e &= \begin{bmatrix} 1 & 0 & 0 & 0 \\ 0 & 0.9995324 & 0 & -0.03057725 \\ 0 & 0 & 1 & 0 \\ 0 & -0.03057725 & 0 & 0.9995324 \end{bmatrix}, \\
 U_R^e &= \begin{bmatrix} 1 & 0 & 0 & 0 \\ 0 & 1 & 0 & -2.49847944 \times 10^{-5} \\ 0 & 0 & 1 & 0 \\ 0 & -2.49847944 \times 10^{-5} & 0 & 1 \end{bmatrix}, & U_R^e &= \begin{bmatrix} 1 & 0 & 0 & 0 \\ 0 & 1 & 0 & -5.423780 \times 10^{-6} \\ 0 & 0 & 1 & 0 \\ 0 & -5.423780 \times 10^{-6} & 0 & 1 \end{bmatrix}, \\
 U_\nu &= \begin{bmatrix} U_{\text{PMNS}} & 0 \\ 0 & 1 \end{bmatrix},
 \end{aligned} \tag{25}$$

where, once again, the blue and black charged lepton mixing matrices correspond to the stars of the same colour in the bottom panel of Fig. 6.

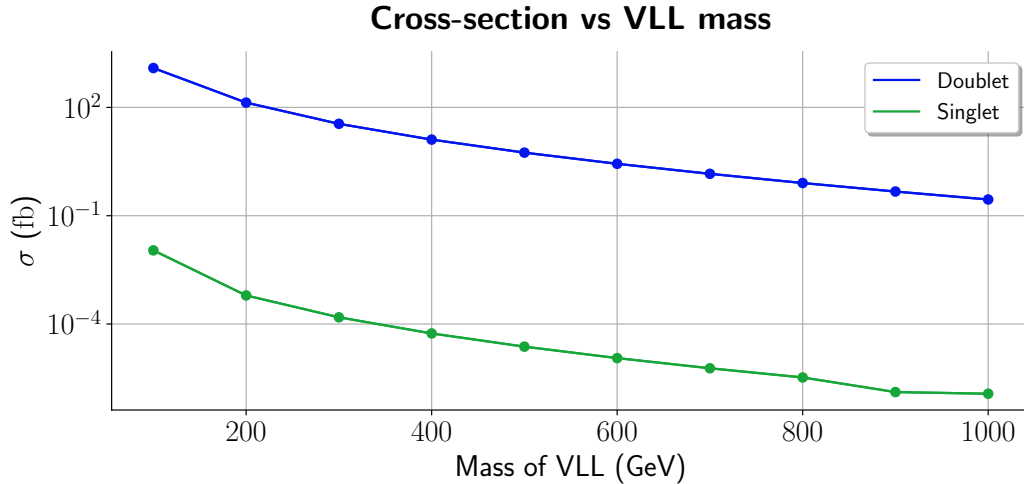


Figure 8: Single production cross section, in femtobarn (fb), as a function of the VLL's mass, in GeV. The y -axis is shown in logarithmic scale.

It follows from Eq. (21) and the numerical values shown above that, upon applying the selection criteria described

in Section III B, the signal and background cross sections are

$$\begin{aligned}\sigma(\text{doublet}) &: 0.39 \text{ fb}, \\ \sigma(\text{singlet}) &: 5.94 \times 10^{-6} \text{ fb}, \\ \sigma(pp \rightarrow \mu^- \bar{\nu}_\mu + \text{up to 2 jets}) &: 4.79 \times 10^6 \text{ fb}.\end{aligned}$$

It is evident that the doublet model cross section is far larger than that of the singlet. This is indeed expected as the dominant contribution in the singlet model contains a $\sin \alpha$ suppression factor as one can see in Eq. (21). The dependency of the production cross section with the VLL mass is shown in Fig. 8.

One can now estimate the total expected number of events, given the cross section above, after event selection. Assuming the target luminosity of the HL-LHC, $\mathcal{L} = 3000 \text{ fb}^{-1}$ and that the expected number of events is given by $N = \sigma \mathcal{L}$, we have for the doublet case $N = 1170$ events, while for the singlet we obtain $N = 0.01782$ events. For the singlet model, this implies that the production cross section is not large enough to generate one event at the LHC. For this reason it is meaningless to present the statistical significance for the singlet model for such a heavy VLL. However, we see from Fig. 8 that, for lighter singlet VLLs, in particular for their masses of 100 and 200 GeV, one has $N \approx 30$ and $N \approx 3$, respectively. Thus, it becomes possible to produce them at the HL-LHC motivating a further full analysis.

The kinematic features used in the Deep Learning analysis can be seen in Figs. 12 and 13 of Appendix B for the doublet and singlet models, respectively. For comparison purposes the signal distributions for both cases are represented together in Fig. 14. Common to both the singlet and doublet models, the main variables allowing for a good discrimination between the signal and the background are the transverse momentum of the muon and of the W boson i.e., $p_T(\mu^-)$ and $p_T(W^-)$, respectively, as well as the MET distribution. These distributions are characterized by long tails at higher energies where the SM background is no longer present. On the other hand, the angular distributions for the cosine of the polar angle, as well as the azimuthal angle, offer the least discriminating power. This follows from the fact that both signal and background have a similar shape. The pseudo-rapidity distributions can also be used in the discrimination since signal events tend to peak around $\eta \sim 0$ whereas the SM backgrounds spread out over the entire $|\eta| \leq 2.5$ region. In particular, for the $\eta(\mu^-)$ distributions, the SM backgrounds spread uniformly in the entire range, while for the case of $\eta(W^-)$, the SM backgrounds show a double-peaked structure with a local minimum around $\eta(W^-) = 0$. This behaviour is identical for both the singlet and doublet frameworks.

Interestingly, looking at Fig. 14, we note that in the MET distributions, the singlet model shows a wider pattern compared to the doublet model, potentially offering a characteristic signature that can be used to distinguish between the different models. Such deviation may be due to the different coupling structure between the singlet and the doublet as noted in Eq. (21). With this information at hand, one can construct multi-dimensional distributions to be used as inputs for a neural network that solves a classification task. This is done via an evolution algorithm to optimise the various hyper-parameters of the neural model, whose metric to be maximised is the Asimov statistical significance. For completeness, we present our results for different statistical models, some more conservative than others. In this article we use the same measures as in [25, 26], which include:

1. The Asimov significance, \mathcal{Z}_A , with 1% systematic uncertainty, as defined in Eq. (22);
2. A less conservative version of the Asimov significance, which we dub as $\mathcal{Z}(< 1\%)$. In this measure, we assume that backgrounds are known with an error of 10^{-3} . Of all measures, this is the most lenient one and typically offers the most significant results;
3. The more traditional metric, $s/\sqrt{s+b}$.

With this in mind, we compute the significances, for the doublet scenario, in a wide range of masses, from 100 to 1000 GeV, in steps of 100 GeV. In particular, we plot the various metrics as a function of the neural network score in Fig. 9, taking a VLL mass equal to 700 GeV, for illustration purposes. For this mass point and, for an integrated luminosity of $\mathcal{L} = 3000 \text{ fb}^{-1}$, we obtain

$$\begin{aligned}s/\sqrt{s+b} &= 34.20\sigma, \\ \mathcal{Z}(< 1\%) &= 48.36\sigma, \\ \mathcal{Z}_A &= 0.96\sigma,\end{aligned}$$

where we immediately notice that we cross the 5σ level for discovery in two of the considered metrics with the exception being the Asimov significance. Indeed, this last one is the stringiest and most conservative one and typically provides the smaller contributions. Due to the high values for the other two metrics, it is interesting to study the role of different values of the luminosity. As such, in Fig. 10, we show the evolution of the significance as a function of the

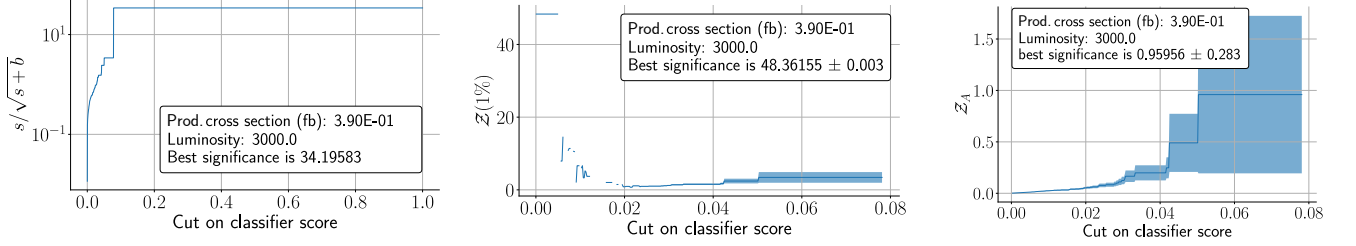


Figure 9: Statistical significance as a function of the classifier score given by a neural network for different metrics, assuming a doublet-type VLL with $M_{\text{VLL}} = 700$ GeV and a collider luminosity $\mathcal{L} = 3000 \text{ fb}^{-1}$. The computation of the statistical significance is made using the best neural network that the evolution algorithm found. From left to right we plot the the significance $s/\sqrt{s+b}$ in (a), the adapted Asimov significance where we assume a background uncertainty of 10^{-3} in (b), and the Asimov significance with systematics of 1% in (c).

collider’s luminosity for a VLL with a mass of 700 GeV. In particular, we highlight with dashed black vertical lines the target luminosities at Run III (300 fb^{-1}) and at the HL-LHC (3000 fb^{-1}). Focusing on Run III, we obtain

$$\begin{aligned} s/\sqrt{s+b} &= 10.81\sigma, \\ \mathcal{Z}(< 1\%) &= 15.29\sigma, \\ \mathcal{Z}_A &= 0.10\sigma, \end{aligned}$$

indicating that one must be able to probe the doublet model for 700 GeV VLLs in the very near future.

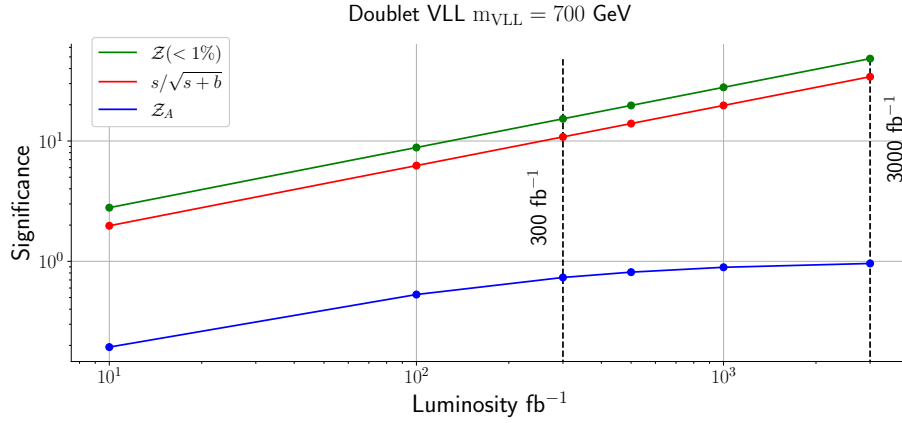


Figure 10: Statistical significance as a function of the collider luminosity, for a fixed doublet VLL mass of 700 GeV. Target luminosities of the HL-LHC (3000 fb^{-1}) and Run III (300 fb^{-1}) are marked with vertical dashed black lines. Both axes are shown in logarithmic scale.

For a more inclusive picture we perform a mass scan constrained to the range $M_{\text{VLL}} \in [100, 1000]$ GeV. All relevant mixing angles are fixed as in Eqs. (24) and (25), chosen in order to optimize the consistency with the $(g-2)_\mu$ anomaly. In particular, we consider, for the doublet model, points belonging to the black line in Fig. 5 for masses up to 500 GeV. The corresponding mixing angles are indicated by the black matrices in Eq. (24). If the doublet mass is equal or larger than 600 GeV we consider points belonging to the blue line in the same figure. For the latter, the mixing angles of the charged lepton sector can be seen in the blue matrices of Eq. (24). On the other hand, it follows from the discussion in the previous paragraphs that only two example points are selected for the singlet model. These belong to the blue line in the bottom panel of Fig. 5 and the mixing angles are shown in blue in Eq. (25). The mass of the right-handed neutrino remains fixed at 100 keV whereas the remaining neutrinos share the same mass with their charged $\text{SU}(2)_L$ doublet counterpart. In Tab. V our results for the scan are summarized, where the VLL masses, the corresponding Δa_μ value and the calculated significance for both Run III and the HL-LHC upgrade are shown. We notice that, both for $\mathcal{L} = 3000 \text{ fb}^{-1}$ or $\mathcal{L} = 300 \text{ fb}^{-1}$ as well as any of the mass values, we are able to consistently

Mass of VLL (GeV)	300 fb ⁻¹			3000 fb ⁻¹			Δa_μ
	$s/\sqrt{s+b}$	$\mathcal{Z}(<1\%)$	\mathcal{Z}_A	$s/\sqrt{s+b}$	$\mathcal{Z}(<1\%)$	\mathcal{Z}_A	
100	604.49	899.31	570.48	1911.55	2858.26	652.44	5.19×10^{-9}
200	201.86	285.55	150.83	638.33	902.98	181.21	3.54×10^{-9}
300	102.57	145.18	52.98	324.37	459.09	66.18	2.60×10^{-9}
400	43.37	87.71	11.20	137.16	277.36	14.42	2.04×10^{-9}
500	36.78	57.93	8.17	116.31	183.20	10.57	1.67×10^{-9}
600	15.24	21.55	1.44	48.20	68.16	1.88	3.03×10^{-9}
700	10.81	15.29	0.1	34.20	48.36	0.96	2.62×10^{-9}
800	7.37	10.64	0.34	23.30	33.66	0.45	2.30×10^{-9}
900	6.11	8.64	0.24	19.33	27.34	0.31	2.06×10^{-9}
1000	4.70	6.65	0.14	14.86	21.02	0.18	1.86×10^{-9}
100	5.45	9.52	0.13	17.24	30.09	0.16	2.94×10^{-9}
200	1.49	2.10	0.010	4.70	6.65	0.012	2.01×10^{-9}

Table V: Signal significance for VLL single-production at the LHC calculated with an evolution algorithm that maximises the Asimov metric. The last two rows represent the singlet model whereas the remaining ten are benchmark points of the doublet model. In the last column we show the corresponding value of Δa_μ .

obtain significances greater than 5σ if the simplified Asimov metric and $s/\sqrt{s+b}$ are considered. These results may indeed suggest that, significances above 5σ can be achievable even for larger VLL mass values at the LHC. This is particularly relevant in the doublet model while for singlet VLLs the significance quickly drops if we go beyond 200 GeV. If only the Asimov significance, \mathcal{Z}_A , which is the most conservative one, is considered we can still probe doublet VLLs up to about 500 GeV already at the LHC Run III. For the singlet scenario, considering the HL-LHC program, we can exclude/discover VLLs up to about 200 GeV with a significance of 6.7 standard deviations for the $\mathcal{Z}(<1\%)$ metric. Although LEP constraints have already excluded VLLs up to 100.6 GeV, our results for 100 GeV are merely indicative. The message to take is that, singlet VLL masses not far above the LEP limit can already be tested at the LHC Run III luminosities. Note also that, in the first row, the value of Δa_μ is excessive. However, we keep such a point as an illustration of how large can the significance become for small doublet masses, if our analysis technique is employed.

The low cross-sections of the singlet model call for a different approach on how to probe them. It is in this context that the near future electron and muon colliders can offer new opportunities. As it was mentioned in Sec. III B, production of particles via electroweak processes is favoured in these colliders. As such, it is instructive to understand how can a lepton collider enhance the cross-section for the case of pair-produced VLLs via an s -channel process. Note that the analysis that follows is independent of the chosen collider, as the s -channel cross-section is independent of the mass of the initial colliding particles. Therefore, all results shown here are valid both for the electron and muon machines. At LO, the main diagrams involved are shown in Fig. 4. Note that, since we are assuming non-zero couplings between the muon/electron and the VLL, there are also t -channel contributions of the form

$$\begin{array}{c}
e^+/\mu^+ \\
\swarrow \quad \searrow \\
\bullet \quad \bullet \\
\gamma \\
\swarrow \quad \searrow \\
e^-/\mu^- \quad E \quad \bar{E}
\end{array}
+
\begin{array}{c}
e^+/\mu^+ \\
\swarrow \quad \searrow \\
\bullet \quad \bullet \\
Z^0 \\
\swarrow \quad \searrow \\
e^-/\mu^- \quad E \quad \bar{E}
\end{array}
. \quad (26)$$

However, such contributions are sub-leading when compared to production via the s -channel process, since these depend on mixing structures of the VLL with the muon, whereas in the s -channel the interaction vertices feature two leptons of the same flavour coupling directly to vectors via gauge interactions. Furthermore, in the particular case of our models, the approximate family symmetry that only allows couplings between muons and VLLs results in vanishing t -channel contributions at electron colliders, but not at muon machines. Note that this channel can be seen as a direct probe to the flavour structure in the leptonic sector if both muon and electron colliders become operational.

Cross-section vs Centre of mass energy

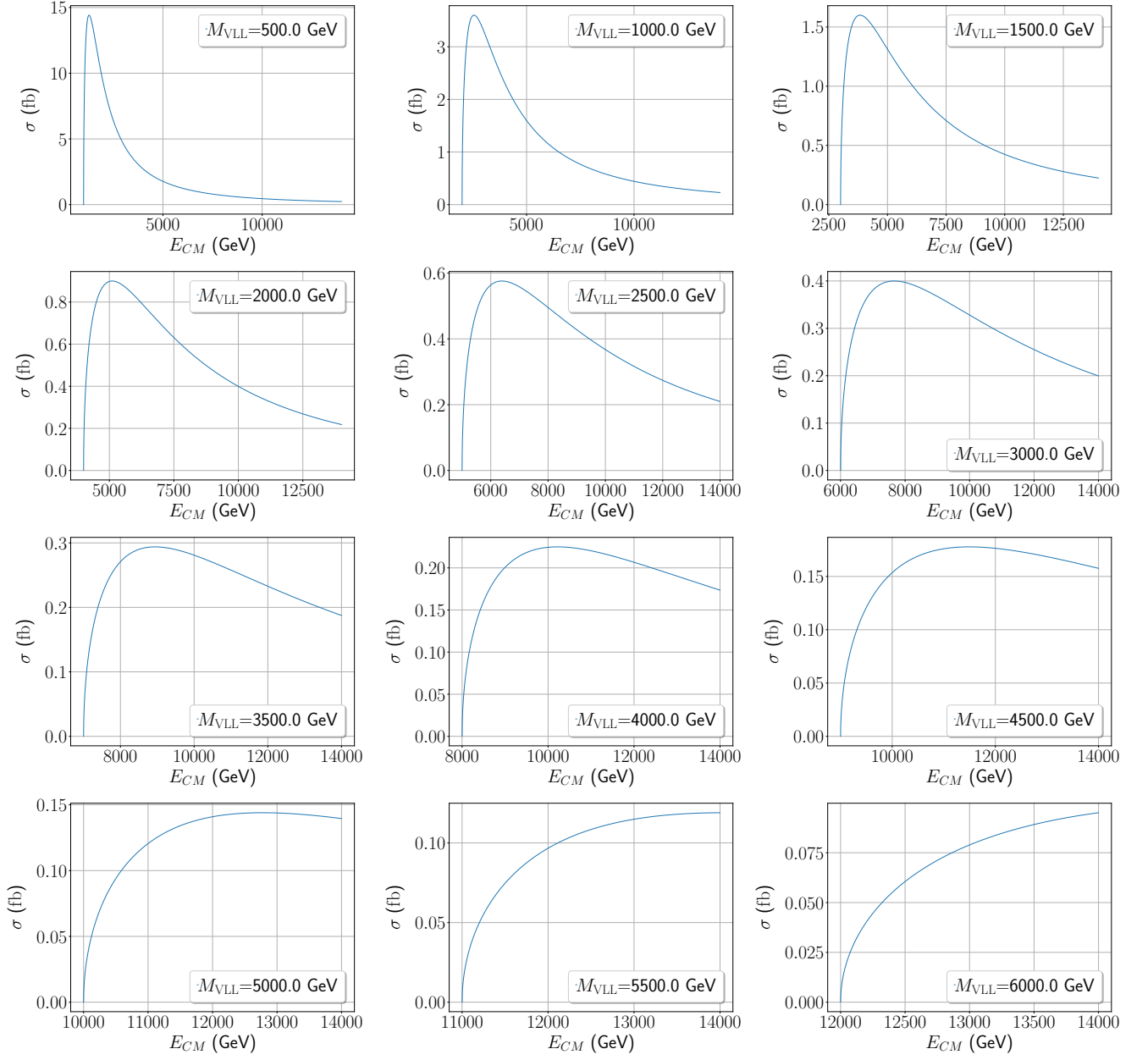


Figure 11: VLL pair production cross section, in fb, as a function of centre-of-mass energy for a lepton collider, in GeV. Each individual box is representative of a different mass of the singlet VLL, which is also given in GeV.

It is then safe to neglect the t -channel contribution in the remainder of this analysis, where we use the same mixing structure as defined in Eq. (25).

For a comprehensive understanding on how the cross section depends on a lepton collider center-of-mass energy, E_{CM} , we use `FeynCalc` to obtain the following expression

$$\sigma = \frac{\sqrt{\frac{E_{\text{CM}}^2}{4} - M_{\mathcal{E}}^2}}{256\pi E_{\text{CM}}^7 (M_{Z^0}^2 - E_{\text{CM}}^2)^2} (\alpha_1 E_{\text{CM}}^8 + \alpha_2 E_{\text{CM}}^6 M_{\mathcal{E}}^2 + \alpha_3 E_{\text{CM}}^6 M_{Z^0}^2 + \alpha_4 E_{\text{CM}}^4 M_{Z^0}^2 M_{\mathcal{E}}^2 + \alpha_5 E_{\text{CM}}^4 M_{Z^0}^4 + \alpha_6 E_{\text{CM}}^2 M_{Z^0}^4 M_{\mathcal{E}}^2), \quad (27)$$

	200 GeV	700 GeV	1200 GeV	1700 GeV	2200 GeV	2700 GeV	3200 GeV	3700 GeV
$E_{\text{CM}} = 1.5 \text{ TeV}$	19.18 fb	5.51 fb	—	—	—	—	—	—
$E_{\text{CM}} = 3 \text{ TeV}$	5.00 fb	4.21 fb	2.49 fb	—	—	—	—	—
$E_{\text{CM}} = 10 \text{ TeV}$	0.46 fb	0.45 fb	0.44 fb	0.41 fb	0.39 fb	0.35 fb	0.31 fb	0.26 fb
$E_{\text{CM}} = 14 \text{ TeV}$	0.23 fb	0.23 fb	0.23 fb	0.22 fb	0.21 fb	0.21 fb	0.19 fb	0.18 fb
$E_{\text{CM}} = 14 \text{ TeV } (e^+e^-\gamma\gamma)$	17.95 fb	0.54 fb	0.095 fb	0.027 fb	0.0095 fb	0.0037 fb	0.001585 fb	0.00069 fb
$E_{\text{CM}} = 14 \text{ TeV } (\mu^+\mu^-\gamma\gamma)$	9.10 fb	0.26 fb	0.045 fb	0.012 fb	0.0043 fb	0.0017 fb	0.00070 fb	0.00030 fb

Table VI: Production cross-section for double production of VLLs at lepton colliders for various masses. We show the cross-section for three distinct points for the centre-of-mass energy $E_{\text{CM}} = 1.5$ and 3 TeV, that correspond to target energies for the CLIC collider, whereas $E_{\text{CM}} = 3, 10$ and 14 TeV correspond to target energies for the future $\mu^+\mu^-$ collider. Points marked with “—” indicate that there is not enough energy to pair-produce the particles at that mass.

where α_i for $i = 1, \dots, 6$ are dimensionless constants, proportional to the product of various couplings, i.e. $\alpha_j = \alpha_j(U_L^e, U_R^e, g, g', \theta_W)$, M_{Z^0} is the mass of the Z^0 boson and $M_{\mathcal{E}}$ the mass of the singlet VLL. With the numerical values in Eq. (25) these constants read as

$$\alpha_1 = 0.189325, \quad \alpha_2 = -0.213435, \quad \alpha_3 = -0.328608, \quad \alpha_4 = 0.403093, \quad \alpha_5 = 0.152126, \quad \alpha_6 = -0.209655. \quad (28)$$

In Fig. 11 we plot the corresponding cross-section as a function of the centre-of-mass energy, for VLL masses in the range between 500 GeV and 6 TeV. Do note that we are studying the singlet scenario, where the decay width always remain below the mass of the VLL. It is interesting to note that the cross sections are rather large, above 13.23 fb for a VLL mass of 500 GeV and $E_{\text{CM}} = 1.5$ TeV, dropping to 0.095 fb for a VLL mass of 6 TeV and $E_{\text{CM}} = 14$ TeV. This increase of the cross section allows to probe higher mass ranges than the ones at the reach of the LHC, in a much cleaner environment. Immediately noticeable is the fact that the cross section hits a maximum shortly after $E_{\text{CM}} \sim 2M_{\text{VLL}}$, with a subsequent drop as E_{CM} increases. This implies that when the collider beam energy is two times the mass of the VLL, the double production of VLL is enhanced and the discovery potential is maximized. For lower masses, the drop is more pronounced when compared to the high-mass regime, essentially because we are taking E_{CM} in the range of 3 – 14 TeV for low masses, while for high masses it occurs for much higher centre-of-mass energies (beyond $E_{\text{CM}} = 14$ TeV), and therefore not as relevant for the proposed lepton colliders. In particular, for $M_{\text{VLL}} = 500$ GeV and at $E_{\text{CM}} = 14$ TeV we have $\sigma = 0.23$ fb, while for the same mass, at $E_{\text{CM}} = 3$ TeV, we have $\sigma = 4.63$ fb. Fixing the centre-of-mass energy and looking at various mass points, as shown in Tab. VI, we notice that for the proposed high-energy colliders, the variation of the mass does not cause significant deviations in the cross-section. For example, taking $E_{\text{CM}} = 14$ TeV, we observe that the cross-section remains nearly constant for the displayed masses, ranging from 0.23 fb for a 200 GeV VLL to 0.18 fb for a 3.7 TeV one.

We end this section with a comment about the cross-sections at the high energy end of the colliders. As the energy grows the s -channel cross sections decrease. However, there is an alternative process that grows with $\ln^2(s/m_f^2)$, where f stands for the incoming fermion. This is $e^+e^- \rightarrow e^+e^-E(\mathcal{E})\bar{E}(\bar{\mathcal{E}})$ for an electron-positron collider and $\mu^+\mu^- \rightarrow \mu^+\mu^-E(\mathcal{E})\bar{E}(\bar{\mathcal{E}})$ for a muon collider. The photon fusion processes have cross-sections that grow with the centre-of-mass energy [41, 42] and although they are not competitive for the lower energies they become dominant at high energies. We present in Tab. VI the values of these cross-sections for an energy of 14 TeV which shows that they can play an important role for very high energy lepton colliders.

V. CONCLUSIONS

In this paper, we performed phenomenological studies of two simple SM extensions containing VLL particles. One with a $\text{SU}(2)_L$ -doublet VLL and the other with a $\text{SU}(2)_L$ -singlet VLL, and in addition both these models are supplemented with an extra right-handed neutrino. Basic phenomenological implications for collider searches were considered, namely, for lepton colliders and the LHC, where for the latter we employed Deep Learning techniques to compute the statistical significance of a hypothetical discovery. We also performed an analysis of the implications of the VLL in addressing the observed discrepancy in the muon anomalous magnetic moment and determined constraints in the Higgs couplings for it to be consistent with the current experimental bounds. We also showed that, if couplings with a neutrino are significant, then the VLLs possess a large decay width, which for certain cases, can become higher than the mass itself.

In the context of the muon $g - 2$ analysis, we performed numerical simulations by computing the contributions of the VLL to the $(g - 2)_\mu$ anomaly. We show that, for the mass range from $M = 100$ GeV to 1000 GeV, both the singlet and doublet models can successfully accommodate the observed discrepancy within a 1σ band. Taking into

consideration that the Z^0 contribution is subleading compared to the Higgs one, limits on the product $g_L^H g_R^H$ for the Higgs couplings are determined, where for a mass of 100 GeV for the VLL, we have $g_L^H g_R^H \in [6.93 \times 10^{-4}, 2.01 \times 10^{-3}]$, while for $M = 1$ TeV we have $g_L^H g_R^H \in [4.14 \times 10^{-3}, 1.15 \times 10^{-2}]$.

In the context of the LHC studies, we perform Monte-Carlo simulations to generate simulated data for signal and background topologies for two benchmark scenarios that are consistent with the $(g - 2)_\mu$ experimental constraints. The signal is characterized by the presence of a single isolated lepton and a substantial amount of MET. To separate the signal from the background, we constructed neural networks which follow from an implementation of evolution algorithm that maximises the Asimov significance. We have shown that, for doublet VLLs, we can exclude masses of VLLs from 100 GeV until 1 TeV with greater than five standard deviations. In particular, for masses of 1 TeV, we obtain significances $s/\sqrt{s+b} = 13.02\sigma$, $\mathcal{Z}(< 1\%) = 18.41\sigma$ and $\mathcal{Z}_A = 0.14\sigma$ for the high luminosity phase of the LHC, with an integrated luminosity of $\mathcal{L} = 3000 \text{ fb}^{-1}$. Within the same mass range, we can also exclude for doublet VLLs for the Run III of the LHC, at $\mathcal{L} = 300 \text{ fb}^{-1}$. At this luminosity, and for a mass of 1 TeV, we have $s/\sqrt{s+b} = 4.11\sigma$, $\mathcal{Z}(< 1\%) = 5.82\sigma$ and $\mathcal{Z}_A = 0.11\sigma$. For the singlet scenario, production cross-sections are substantially lower and the expected number of events is usually zero, with an exception of the mass points of 100 GeV and 200 GeV. For the first one, we find the significance to be $s/\sqrt{s+b} = 5.34\sigma$, $\mathcal{Z}(< 1\%) = 8.11\sigma$ and $\mathcal{Z}_A = 0.016\sigma$ at $\mathcal{L} = 3000 \text{ fb}^{-1}$, and $s/\sqrt{s+b} = 1.69\sigma$, $\mathcal{Z}(< 1\%) = 2.57\sigma$ and $\mathcal{Z}_A = 0.013\sigma$ at $\mathcal{L} = 300 \text{ fb}^{-1}$, indicating that singlet VLLs can only start to be excluded at the high-luminosity phase of the LHC. For the second point, with a 200 GeV VLL, an exclusion can not be determined.

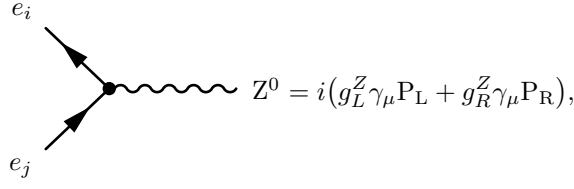
Owning to the low production cross-sections of the singlet scenario, a supplementary analysis is made within the context of lepton colliders. We perform numerical computations for the expected cross-section for pair-production of VLLs in the s -channel. We find that greater cross-sections can be obtained when compared to the LHC analysis, allowing for a much wider range of masses to be probed. In particular, we find that the highest cross-sections are obtained for low centre-of-mass energies. In particular, for a VLL mass of $M_{\text{VLL}} = 200$ GeV, we obtain a cross-section of $\sigma = 13.23 \text{ fb}$ for $E_{\text{CM}} = 1.5$ TeV, while $\sigma = 0.095 \text{ fb}$ for energy $E_{\text{CM}} = 14$ TeV.

Acknowledgements. J.G., F.F.F., and A.P.M. are supported by the Center for Research and Development in Mathematics and Applications (CIDMA) through the Portuguese Foundation for Science and Technology (FCT - Fundação para a Ciência e a Tecnologia), references UIDB/04106/2020 and UIDP/04106/2020. A.P.M., F.F.F., J.G. and R.S. are supported by the project PTDC/FIS-PAR/31000/2017. A.P.M. is also supported by national funds (OE), through FCT, I.P., in the scope of the framework contract foreseen in the numbers 4, 5 and 6 of the article 23, of the Decree-Law 57/2016, of August 29, changed by Law 57/2017, of July 19. R.P. is supported in part by the Swedish Research Council grant, contract number 2016-05996, as well as by the European Research Council (ERC) under the European Union's Horizon 2020 research and innovation programme (grant agreement No 668679). R.S. is supported by CFTC-UL under FCT contracts UIDB/00618/2020, UIDP/00618/2020, and by the projects CERN/FISPAR/0002/2017, CERN/FIS-PAR/0014/2019 and by the HARMONIA project of the National Science Centre, Poland, under contract UMO- 2015/18/M/ST2/00518. A.O. is supported by the FCT project CERN/FIS-PAR/0029/2019.

Appendix A: Feynman Rules

In this appendix, the list of Feynman rules relevant for the numerical analysis is presented. All rules are displayed in the mass basis. To simplify the notation, we define the chirality projection operators as $P_L = (1 - \gamma_5)/2$ and $P_R = (1 + \gamma_5)/2$. Notation wise, we define the following: θ_W is the Weinberg mixing angle, g the $SU(2)_L$ gauge coupling and g' the $U(1)_Y$ gauge coupling. The Latin indices $i, j = (1, 2, 3, 4)$ denote $(e, \mu, \tau, E(\mathcal{E}))$ for leptons, while for neutrinos $i, j = (1, 2, 3, 4, 5, 6) = (\nu_1, \nu_2, \nu_3, \nu_4, \nu_5, \nu_6)$, with ν_5 and ν_6 arising from the doublet representation of the VLL and ν_4 is the sterile neutrino. For the singlet model, there is no extra left-handed neutrinos, hence the latin indices only run from 1 to 4.

For the doublet case, the Feynman rules read as

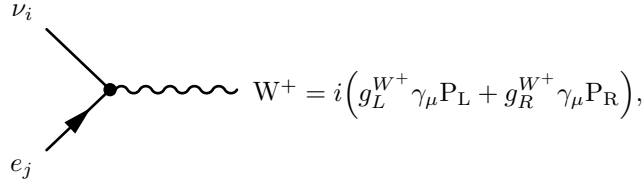


$$Z^0 = i(g_L^Z \gamma_\mu P_L + g_R^Z \gamma_\mu P_R),$$

(A1)

$$g_L^Z = \frac{1}{2}(g \cos \theta_W - g' \sin \theta_W) \left[(U_L^e)^*_{j4} (U_L^e)_{i4} + \sum_{a=1}^3 (U_L^e)^*_{ja} (U_L^e)_{ia} \right],$$

$$g_R^Z = -g' \sin(\theta_W) \sum_{a=1}^3 (U_R^e)^*_{ia} (U_R^e)_{ja} + \frac{1}{2} (U_R^e)^*_{i4} (U_R^e)_{j4} (g \cos \theta_W - g' \sin \theta_W),$$

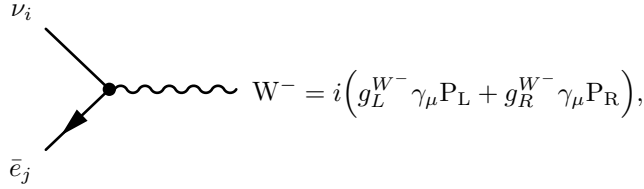


$$W^+ = i(g_L^{W^+} \gamma_\mu P_L + g_R^{W^+} \gamma_\mu P_R),$$

(A2)

$$g_L^{W^+} = -\frac{g}{\sqrt{2}} \left[(U_L^e)^*_{j4} (U_\nu)_{i4} + \sum_{a=1}^3 (U_L^e)^*_{ja} (U_\nu)_{ia} \right],$$

$$g_R^{W^+} = -\frac{g}{\sqrt{2}} (U_\nu)^*_{i5} (U_R^e)_{j4},$$

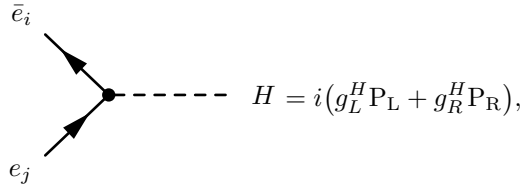


$$W^- = i(g_L^{W^-} \gamma_\mu P_L + g_R^{W^-} \gamma_\mu P_R),$$

(A3)

$$g_L^{W^-} = -\frac{g}{\sqrt{2}} \left[(U_\nu)^*_{i4} (U_L^e)_{j4} + \sum_{a=1}^3 (U_\nu)^*_{ia} (U_L^e)_{ja} \right],$$

$$g_R^{W^-} = -\frac{g}{\sqrt{2}} (U_R^e)^*_{j4} (U_\nu)_{i5},$$



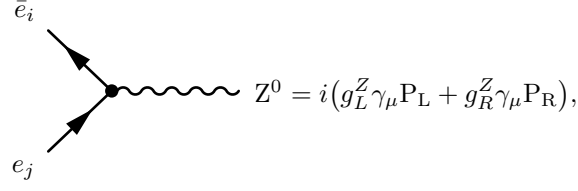
$$H = i(g_L^H P_L + g_R^H P_R),$$

(A4)

$$g_L^H = \frac{1}{\sqrt{2}} \left[\sum_{a=1}^3 (U_L^e)^*_{j4} (U_R^e)^*_{ia} \Theta_a + \sum_{a=1}^3 \sum_{b=1}^3 (U_R^e)^*_{ib} (U_L^e)^*_{ja} \Pi_{ab} \right],$$

$$g_R^H = \frac{1}{\sqrt{2}} \left[\sum_{a=1}^3 (U_R^e)_{ja} (U_L^e)_{i4} \Theta_a^* + \sum_{a=1}^3 \sum_{b=1}^3 (U_L^e)_{ia} (U_R^e)_{jb} \Pi_{ab}^* \right],$$

Similarly, for the singlet case we have,

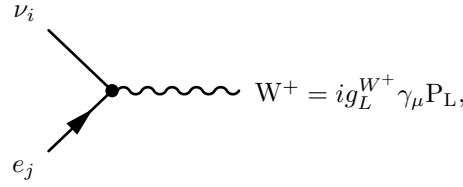


$$Z^0 = i(g_L^Z \gamma_\mu P_L + g_R^Z \gamma_\mu P_R),$$

(A5)

$$g_L^Z = -g'(U_L^e)_{j4}^* (U_L^e)_{i4} \sin(\theta_W) + \frac{1}{2}(g \cos \theta_W - g' \sin \theta_W) \sum_{a=1}^3 (U_L^e)_{ja}^* (U_L^e)_{ia},$$

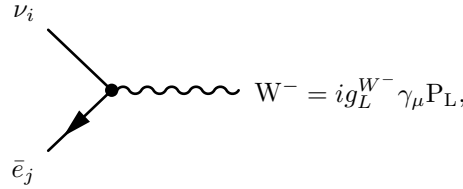
$$g_R^Z = -g' \sin(\theta_W) \left[(U_R^e)_{i4}^* (U_R^e)_{j4} + \sum_{a=1}^3 (U_R^e)_{ia}^* (U_R^e)_{ja} \right],$$



$$W^+ = i g_L^{W+} \gamma_\mu P_L,$$

(A6)

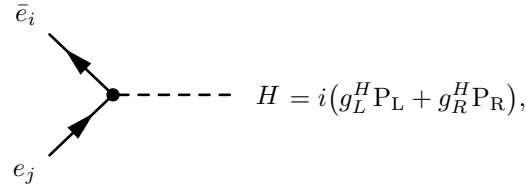
$$g_L^{W+} = -\frac{g}{\sqrt{2}} \sum_{a=1}^3 (U_L^e)_{ja}^* (U_\nu)_{ia},$$



$$W^- = i g_L^{W-} \gamma_\mu P_L,$$

(A7)

$$g_L^{W-} = -\frac{g}{\sqrt{2}} \sum_{a=1}^3 (U_\nu)_{ia}^* (U_L^e)_{ja},$$



$$H = i(g_L^H P_L + g_R^H P_R),$$

(A8)

$$g_L^H = \frac{1}{\sqrt{2}} \left[\sum_{a=1}^3 (U_R^e)_{i4}^* (U_L^e)_{ja}^* \theta_a + \sum_{a=1}^3 \sum_{b=1}^3 (U_R^e)_{ib}^* (U_L^e)_{ja}^* \Pi_{ab} \right],$$

$$g_R^H = \frac{1}{\sqrt{2}} \left[\sum_{a=1}^3 (U_L^e)_{ia} (U_R^e)_{j4} \theta_a^* + \sum_{a=1}^3 \sum_{b=1}^3 (U_L^e)_{ia} (U_R^e)_{jb} \Pi_{ab}^* \right].$$

Appendix B: Kinematic distributions for VLL single-production

Single production of doublet VLL with mass $M = 700$ GeV

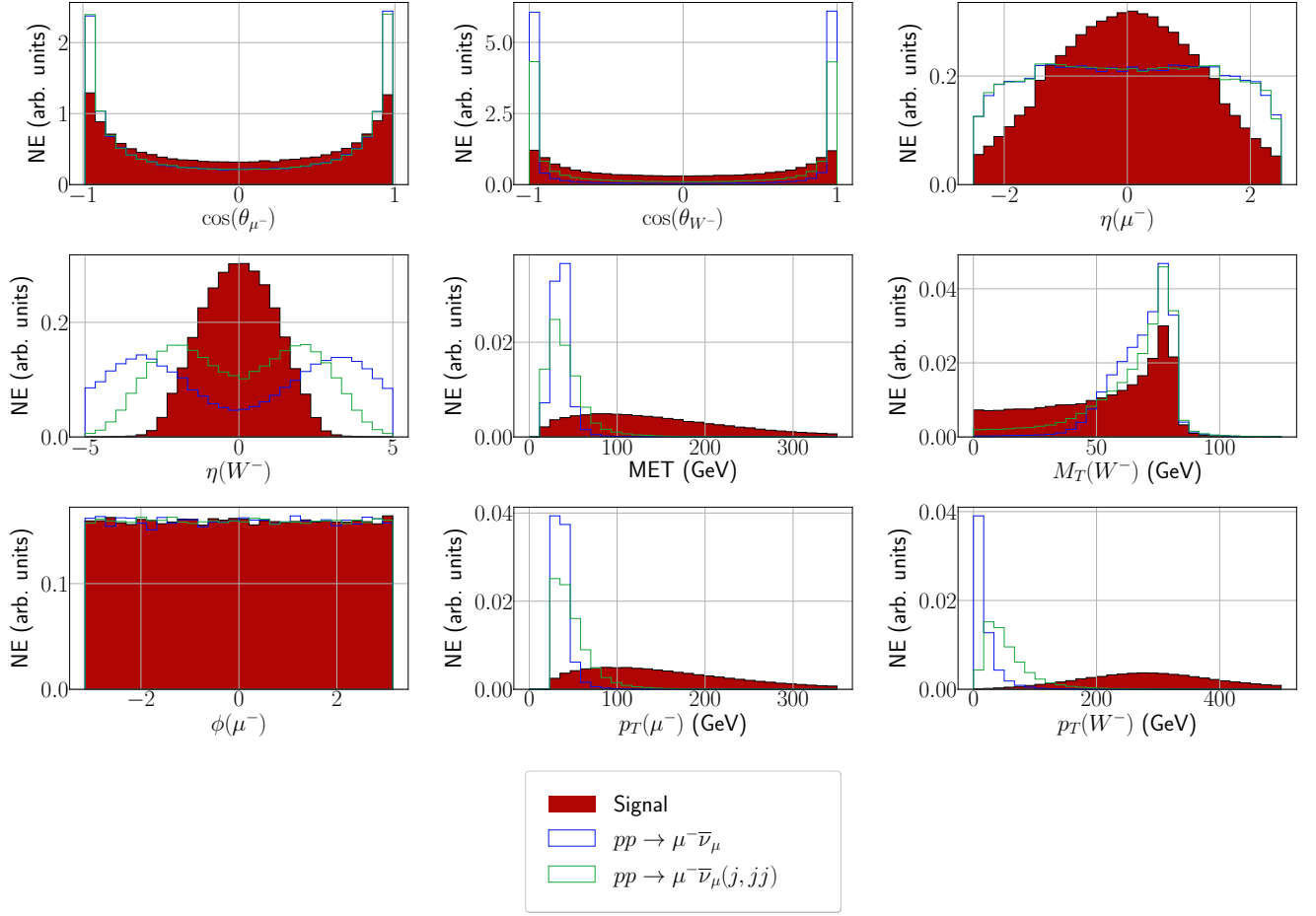


Figure 12: Kinematic variables that the neural network uses for classification. Data is simulated for a doublet VLL with mass of 700 GeV and in the ATLAS detector. From left to right and top to bottom, the variables are $\cos(\theta_{\mu^-})$, $\cos(\theta_{W^-})$, pseudo-rapidity of the muon, reconstructed pseudo-rapidity of W^- , MET, transverse mass of W^- , azimuthal angle of the muon, transverse momentum of the muon and the reconstructed transverse momentum of the W boson. In the y -axis, it is indicated that events are normalized (NE). We consider 30 bins for all background and signal histograms.

Single production of singlet VLL with mass $M = 700$ GeV

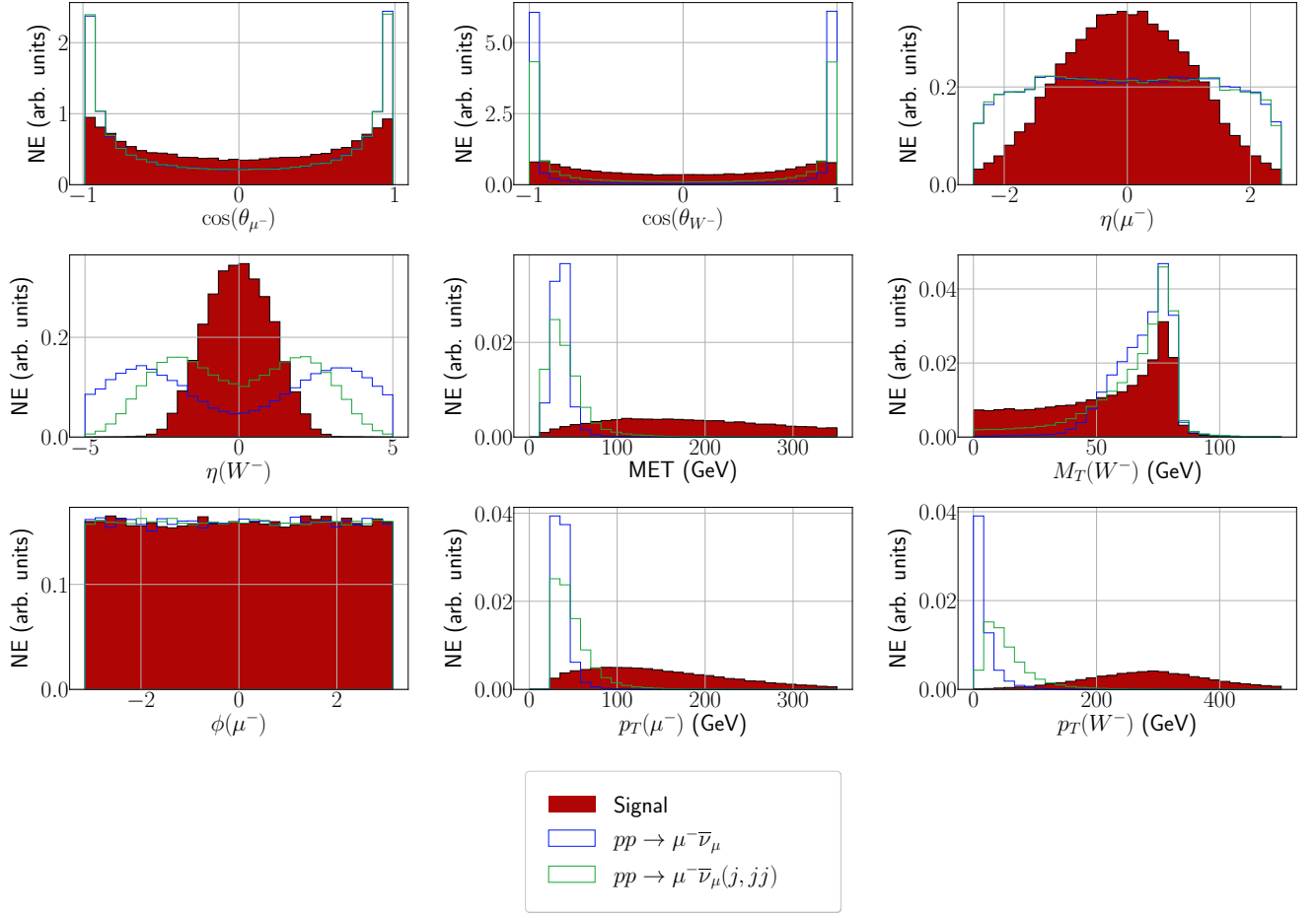


Figure 13: Kinematic variables that the neural network uses for classification. Data is simulated for a singlet VLL with mass of 700 GeV and in the ATLAS detector. The kinematic variables and the corresponding labelling order is identical to the caption of Fig. 12.

Doublet (in blue) and Singlet (in green). Both 700 GeV

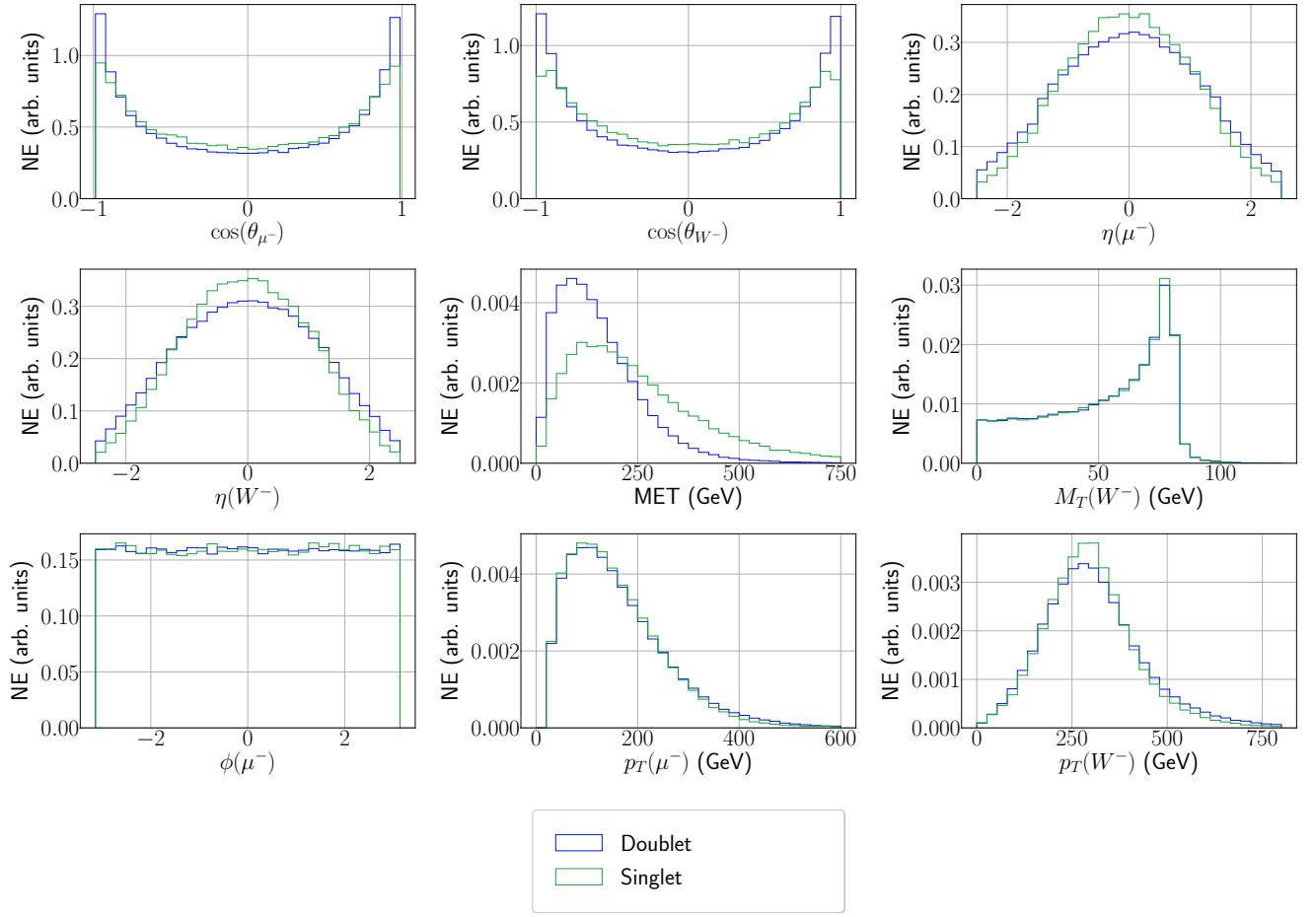


Figure 14: Comparison plots between the kinematic distributions for doublet VLL (in blue) and singlet VLL (in green) single production. The kinematic variables and the corresponding labelling order is identical to the caption of Fig. 12.

Appendix C: Neural networks found via the genetic algorithm

Mass	Doublet
100 GeV	<p>Layers : 1 input + 1 output. Input layer with 256 neurons, output layer with 3 neurons <u>Regularizer</u> : L1L2 (layer 1) and none (layer 2) <u>Activation function</u> : Sigmoid (for layers 1 and 2) <u>Initializer</u> : VarianceScaling, with uniform distribution (layer 1) in fan_in mode and GlorotUniform (layer 2) with null seed</p>
200 GeV	<p>Layers : 1 input + 1 hidden + 1 output. Hidden and input layers with 512 neurons each, output layer with 3 neurons <u>Regularizer</u> : L1L2 (layers 1 and 2) and none (for layer 3) <u>Activation function</u> : sigmoid (all layers) <u>Initializer</u> : VarianceScaling, with truncated normal distribution (layers 1 and 2) in fan_in mode and GlorotUniform distribution (for layers 3) with null seed</p>
300 GeV	<p>Layers : 1 input + 1 output. Input layer with 512 neurons, output layer with 3 neurons <u>Regularizer</u> : L1L2 (for layer 1) and none (for layer 2) <u>Activation function</u> : tanh (for layer 1) and sigmoid (layer 2) <u>Initializer</u> : VarianceScaling, with truncated normal distribution (for layer 1) in fan_in mode and GlorotUniform distribution (layer 2) with null seed</p>
400 GeV	<p>Layers : 1 input + 1 hidden + 1 output. Hidden and input layers with 256 neurons each, output layer with 3 neurons <u>Regularizer</u> : L1L2 (for layers 1 and 2) and none (for layer 3) <u>Activation function</u> : sigmoid (all layers) <u>Initializer</u> : VarianceScaling, with truncated normal distribution (layers 1 and 2) in fan_in mode and GlorotUniform distribution (layer 3) with null seed</p>
500 GeV	<p>Layers : 1 input + 1 output. Input layer with 512 neurons, output layer with 3 neurons <u>Regularizer</u> : L1L2 (layer 1) and none (layer 2) <u>Activation function</u> : sigmoid (all layers) <u>Initializer</u> : VarianceScaling, with truncated normal distribution (layer 1) in fan_in mode and GlorotUniform distribution (layer 2) with null seed</p>

Table VII: Architectures for the neural networks that the genetic algorithm finds for the scanned masses (100 to 500 GeV) of the doublet VLL scenario.

Mass	Doublet
600 GeV	<p><u>Layers</u> : 1 input + 2 hidden + 1 output. Hidden and input layers with 256 neurons each, output layer with 3 neurons <u>Regularizer</u> : L1L2 (for layers 1 to 3) and none (for layer 4) <u>Activation function</u> : sigmoid (for all layers) <u>Initializer</u> : VarianceScaling, with uniform distribution (for layers 1 to 3) in fan_in mode and GlorotUniform distribution (layer 4) with null seed</p>
700 GeV	<p><u>Layers</u> : 1 input + 2 hidden + 1 output. Hidden and input layers with 1024 neurons each, output layer with 3 neurons <u>Regularizer</u> : L1L2 (for layers 1 to 3) and none (for layer 4) <u>Activation function</u> : tanh (for layers 1 to 3) and sigmoid (for layer 4) <u>Initializer</u> : VarianceScaling, with uniform distribution (for layers 1 to 3) in fan_in mode and uniform distribution (layer 4) in fan_avg mode</p>
800 GeV	<p><u>Layers</u> : 1 input + 3 hidden + 1 output. Hidden and input layers with 256 neurons each, output layer with 3 neurons <u>Regularizer</u> : L1L2 (for layers 1 and 4) and none (for layer 5) <u>Activation function</u> : relu (for all layers) <u>Initializer</u> : RandomNormal, with 0 mean and 0.05 standard deviation (for layers 1 to 4) and GlorotUniform distribution (layer 5) with null seed</p>
900 GeV	<p><u>Layers</u> : 1 input + 2 hidden + 1 output. Hidden and input layers with 256 neurons each, output layer with 3 neurons <u>Regularizer</u> : L1L2 (for layers 1 to 3) and none (for layer 4) <u>Activation function</u> : sigmoid (for all layers) <u>Initializer</u> : VarianceScaling, with truncated normal distribution (for layers 1 to 5) in fan_in mode and GlorotUniform distribution (layer 4) with null seed</p>
1000 GeV	<p><u>Layers</u> : 1 input + 2 hidden + 1 output. Hidden and input layers with 1024 neurons each, output layer with 3 neurons <u>Regularizer</u> : L1L2 (for layers 1 to 3) and none (for layer 4) <u>Activation function</u> : tanh (for layers 1 to 3) and sigmoid (layer 4) <u>Initializer</u> : VarianceScaling, with uniform distribution (for layers 1 to 3) in fan_in mode and GlorotUniform distribution (layer 4) with null seed</p>

Table VIII: Architectures for the neural networks that the genetic algorithm finds for the scanned masses (600 to 1000 GeV) of the doublet VLL scenario.

Mass	Singlet
100 GeV	<p><u>Layers</u> : 1 input + 3 hidden + 1 output. Hidden and input layers with 256 neurons each, output layer with 3 neurons</p> <p><u>Regularizer</u> : L1L2 (for layers 1 to 4) and none (for layer 5)</p> <p><u>Activation function</u> : relu (for layers 1 to 4) and sigmoid (for layer 5)</p> <p><u>Initializer</u> : RandomNormal, with 0 mean and 0.05 standard deviation (for layers 1 to 4) and GlorotUniform distribution (layer 5) with null seed</p>
200 GeV	<p><u>Layers</u> : 1 input + 1 hidden + 1 output. Hidden and input layers with 2048 neurons each, output layer with 3 neurons</p> <p><u>Regularizer</u> : L1L2 (for layers 1 and 2) and none (for layer 3)</p> <p><u>Activation function</u> : tanh (for layers 1 and 2) and sigmoid (for layer 3)</p> <p><u>Initializer</u> : VarianceScaling, with uniform distribution (layer 1 and 2) in fan_in mode and GlorotUniform distribution (for layers 3) with null seed</p>

Table IX: Architectures for the neural networks that the genetic algorithm finds for the scanned masses (100 and 200 GeV) of the singlet VLL scenario.

-
- [1] Y. Fukuda et al. (Super-Kamiokande), “Evidence for oscillation of atmospheric neutrinos,” *Phys. Rev. Lett.* **81**, 1562–1567 (1998), [arXiv:hep-ex/9807003](#).
 - [2] Gianfranco Bertone, Dan Hooper, and Joseph Silk, “Particle dark matter: Evidence, candidates and constraints,” *Phys. Rept.* **405**, 279–390 (2005), [arXiv:hep-ph/0404175](#).
 - [3] B. Abi et al. (Muon g-2), “Measurement of the Positive Muon Anomalous Magnetic Moment to 0.46 ppm,” *Phys. Rev. Lett.* **126**, 141801 (2021), [arXiv:2104.03281 \[hep-ex\]](#).
 - [4] Roel Aaij et al. (LHCb), “Test of lepton universality in beauty-quark decays,” (2021), [arXiv:2103.11769 \[hep-ex\]](#).
 - [5] António P. Morais, Roman Pasechnik, and Werner Porod, “Prospects for new physics from gauge left-right-colour-family grand unification hypothesis,” *Eur. Phys. J. C* **80**, 1162 (2020), [arXiv:2001.06383 \[hep-ph\]](#).
 - [6] Francisco J. de Anda, Alfredo Aranda, António P. Morais, and Roman Pasechnik, “Gauge couplings evolution from the Standard Model, through Pati-Salam theory, into E_8 unification of families and forces,” (2020), [arXiv:2011.13902 \[hep-ph\]](#).
 - [7] Alfredo Aranda, Francisco J. de Anda, António P. Morais, and Roman Pasechnik, “A Different Take on E_8 Unification,” (2021), [arXiv:2107.05421 \[hep-ph\]](#).
 - [8] Alfredo Aranda, Francisco J. de Anda, António P. Morais, and Roman Pasechnik, “Sculpting the Standard Model from low-scale Gauge-Higgs-Matter E_8 Grand Unification in ten dimensions,” (2021), [arXiv:2107.05495 \[hep-ph\]](#).
 - [9] Otto Eberhardt, Geoffrey Herbert, Heiko Lacker, Alexander Lenz, Andreas Menzel, Ulrich Nierste, and Martin Wiebusch, “Impact of a Higgs boson at a mass of 126 GeV on the standard model with three and four fermion generations,” *Phys. Rev. Lett.* **109**, 241802 (2012), [arXiv:1209.1101 \[hep-ph\]](#).
 - [10] P. A. Zyla et al. (Particle Data Group), “Review of Particle Physics,” *PTEP* **2020**, 083C01 (2020).
 - [11] Alessandro Strumia and Francesco Vissani, “Neutrino masses and mixings and...” (2006), [arXiv:hep-ph/0606054](#).
 - [12] P. Achard et al. (L3), “Search for heavy neutral and charged leptons in e^+e^- annihilation at LEP,” *Phys. Lett. B* **517**, 75–85 (2001), [arXiv:hep-ex/0107015](#).
 - [13] Albert M Sirunyan et al. (CMS), “Search for vector-like leptons in multilepton final states in proton-proton collisions at $\sqrt{s} = 13$ TeV,” *Phys. Rev. D* **100**, 052003 (2019), [arXiv:1905.10853 \[hep-ex\]](#).
 - [14] Ivan Esteban, M. C. Gonzalez-Garcia, Michele Maltoni, Thomas Schwetz, and Albert Zhou, “The fate of hints: updated global analysis of three-flavor neutrino oscillations,” *JHEP* **09**, 178 (2020), [arXiv:2007.14792 \[hep-ph\]](#).
 - [15] V. Kuksa and N. Volchanskiy, “Factorization in the model of unstable particles with smeared mass,” *Central Eur. J. Phys.* **11**, 182–194 (2013), [arXiv:1109.1541 \[hep-ph\]](#).
 - [16] V. I. Kuksa, “Convolution formula for decay rate,” *Phys. Lett. B* **633**, 545–549 (2006), [Erratum: *Phys.Lett.B* 664, 315 (2008)], [arXiv:hep-ph/0508164](#).
 - [17] V. I. Kuksa, “Factorization method in the model of unstable particles with a smeared mass,” *Phys. Atom. Nucl.* **72**, 1063–1073 (2009), [arXiv:0902.4892 \[hep-ph\]](#).
 - [18] Radovan Dermisek, Keith Hermanek, and Navin McGinnis, “Muon $g - 2$ in two Higgs doublet models with vectorlike leptons,” (2021), [arXiv:2103.05645 \[hep-ph\]](#).
 - [19] Kristjan Kannike, Martti Raidal, David M. Straub, and Alessandro Strumia, “Anthropic solution to the magnetic muon anomaly: the charged see-saw,” *JHEP* **02**, 106 (2012), [Erratum: *JHEP* 10, 136 (2012)], [arXiv:1111.2551 \[hep-ph\]](#).
 - [20] Fred Jegerlehner and Andreas Nyffeler, “The Muon g-2,” *Phys. Rept.* **477**, 1–110 (2009), [arXiv:0902.3360 \[hep-ph\]](#).
 - [21] Radovan Dermisek and Aditi Raval, “Explanation of the Muon g-2 Anomaly with Vectorlike Leptons and its Implications for Higgs Decays,” *Phys. Rev. D* **88**, 013017 (2013), [arXiv:1305.3522 \[hep-ph\]](#).
 - [22] Kevin R. Lynch, “A Note on one loop electroweak contributions to g-2: A Companion to BUHEP-01-16,” (2001), [arXiv:hep-ph/0108081](#).
 - [23] W. Porod and F. Staub, “SPheno 3.1: Extensions including flavour, CP-phases and models beyond the MSSM,” *Comput. Phys. Commun.* **183**, 2458–2469 (2012), [arXiv:1104.1573 \[hep-ph\]](#).
 - [24] David M. Straub, “flavio: a Python package for flavour and precision phenomenology in the Standard Model and beyond,” (2018), [arXiv:1810.08132 \[hep-ph\]](#).
 - [25] Felipe F. Freitas, João Gonçalves, António P. Morais, and Roman Pasechnik, “Phenomenology of vector-like leptons with Deep Learning at the Large Hadron Collider,” *JHEP* **01**, 076 (2021), [arXiv:2010.01307 \[hep-ph\]](#).
 - [26] Cesar Bonilla, A. E. Cárcamo Hernández, João Gonçalves, Felipe F. Freitas, Antonio P. Morais, and R. Pasechnik, “Collider signatures of vector-like fermions from a flavor symmetric 2HDM,” (2021), [arXiv:2107.14165 \[hep-ph\]](#).
 - [27] Florian Staub, “SARAH 4 : A tool for (not only SUSY) model builders,” *Comput. Phys. Commun.* **185**, 1773–1790 (2014), [arXiv:1309.7223 \[hep-ph\]](#).
 - [28] J. Alwall, R. Frederix, S. Frixione, V. Hirschi, F. Maltoni, O. Mattelaer, H. S. Shao, T. Stelzer, P. Torrielli, and M. Zaro, “The automated computation of tree-level and next-to-leading order differential cross sections, and their matching to parton shower simulations,” *JHEP* **07**, 079 (2014), [arXiv:1405.0301 \[hep-ph\]](#).
 - [29] Torbjörn Sjöstrand, Stefan Ask, Jesper R. Christiansen, Richard Corke, Nishita Desai, Philip Ilten, Stephen Mrenna, Stefan Prestel, Christine O. Rasmussen, and Peter Z. Skands, “An introduction to PYTHIA 8.2,” *Comput. Phys. Commun.* **191**, 159–177 (2015), [arXiv:1410.3012 \[hep-ph\]](#).
 - [30] Richard D. Ball, Valerio Bertone, Stefano Carrazza, Luigi Del Debbio, Stefano Forte, Alberto Guffanti, Nathan P. Hartland, and Juan Rojo (NNPDF), “Parton distributions with QED corrections,” *Nucl. Phys. B* **877**, 290–320 (2013), [arXiv:1308.0598 \[hep-ph\]](#).
 - [31] J. de Favereau, C. Delaere, P. Demin, A. Giammanco, V. Lemaître, A. Mertens, and M. Selvaggi (DELPHES 3),

- “DELPHES 3, A modular framework for fast simulation of a generic collider experiment,” *JHEP* **02**, 057 (2014), [arXiv:1307.6346 \[hep-ex\]](#).
- [32] R. Brun and F. Rademakers, “ROOT: An object oriented data analysis framework,” *Nucl. Instrum. Meth. A* **389**, 81–86 (1997).
- [33] François Chollet et al., “Keras,” <https://keras.io> (2015).
- [34] T. K. Charles et al. (CLICdp, CLIC), “The Compact Linear Collider (CLIC) - 2018 Summary Report,” **2/2018** (2018), [10.23731/CYRM-2018-002](#), [arXiv:1812.06018 \[physics.acc-ph\]](#).
- [35] M J Boland et al. (CLIC, CLICdp), “Updated baseline for a staged Compact Linear Collider,” (2016), [10.5170/CERN-2016-004](#), [arXiv:1608.07537 \[physics.acc-ph\]](#).
- [36] “The International Linear Collider Technical Design Report - Volume 2: Physics,” (2013), [arXiv:1306.6352 \[hep-ph\]](#).
- [37] Vladimir Shiltsev, “Muon colliders –opening new horizons for particle physics,” https://indico.cern.ch/event/1022802/contributions/4293870/attachments/2218112/3755618/MuonCollider_UChi_03292021_v1.pdf (2021).
- [38] “Muon collider forum kickoff meeting,” <https://indico.fnal.gov/event/47038/> (2021).
- [39] Vladyslav Shtabovenko, Rolf Mertig, and Frederik Orellana, “FeynCalc 9.3: New features and improvements,” *Comput. Phys. Commun.* **256**, 107478 (2020), [arXiv:2001.04407 \[hep-ph\]](#).
- [40] Kenny C. Y. Ng, Brandon M. Roach, Kerstin Perez, John F. Beacom, Shunsaku Horiuchi, Roman Krivonos, and Daniel R. Wik, “New Constraints on Sterile Neutrino Dark Matter from *NuSTAR* M31 Observations,” *Phys. Rev. D* **99**, 083005 (2019), [arXiv:1901.01262 \[astro-ph.HE\]](#).
- [41] V. M. Budnev, I. F. Ginzburg, G. V. Meledin, and V. G. Serbo, “The Two photon particle production mechanism. Physical problems. Applications. Equivalent photon approximation,” *Phys. Rept.* **15**, 181–281 (1975).
- [42] Stefano Frixione, Michelangelo L. Mangano, Paolo Nason, and Giovanni Ridolfi, “Improving the Weizsacker-Williams approximation in electron - proton collisions,” *Phys. Lett. B* **319**, 339–345 (1993), [arXiv:hep-ph/9310350](#).